https://doi.org/10.5194/egusphere-2026-3869
Preprint. Discussion started: 31 July 2026

Diurnal cycles of deep convective processes: Biases of ERA5 and DYAMOND km-scale models revealed by satellite observations of frozen water path and precipitation

Lara Leko[1,*], Gunnar Behrens[1,*], Nils Müller[1,a], Adrià Amell[1], Axel Lauer[2], and Patrick Eriksson[1]

[1]Chalmers University of Technology, Gothenburg, Sweden
[2]Deutsches Zentrum für Luft- und Raumfahrt (DLR), Institut für Physik der Atmosphäre, Oberpfaffenhofen, Germany
[*]These authors contributed equally to this work.
[a]now at: Alfred-Wegener-Institut, Helmholtz-Zentrum für Polar- und Meeresforschung (AWI), Bremerhaven, Germany

Correspondence: Gunnar Behrens (gunnar.behrens@chalmers.se)

Abstract.

Tropical convective processes show pronounced diurnal variability with strong land and ocean contrasts. Here, we compare their diurnal cycles from satellite observations, ERA5 and km-scale models. As observational base, we use the Chalmers Cloud Ice Climatology (CCIC), a machine-learning satellite product, for frozen water path (FWP) and high cloud cover, and IMERG for precipitation. CCIC captures the full diurnal cycle of FWP in contrast to older satellite FWP products. The satellite observations show late-night or early-morning peaks over the oceans, and afternoon peaks over tropical land areas for FWP and precipitation. The diurnal cycle of tropical FWP and precipitation has a general synchronicity in satellite observations. High cloud cover over tropical land lags behind FWP and precipitation by several hours and peaks during the night in the warm, wet season. ERA5 shows a smaller diurnal amplitude of FWP over tropical land with local phase shifts of more than ±6 hours compared to CCIC. In contrast, the diurnal amplitude of ERA5 precipitation exceeds that of IMERG over land areas and lacks night-time peaks related to mesoscale convective systems and topography. Km-scale models have smaller diurnal phase shifts; however, regional biases exist over the South Pacific Convergence Zone, as well as systematic differences in diurnal amplitudes over tropical land areas, which can be quantified with satellite observations like CCIC. Our analysis illustrates the power of combining different satellite products to better understand the diurnal cycles of tropical convective processes when evaluating reanalyses or models.

1 Introduction

The diurnal cycle of deep convective processes in the tropics is a dominant source of internal variability of the weather and climate system on synoptic timescales in satellite and ground observations (e.g. Song et al., 2024; Dai, 2023; Christopoulos and Schneider, 2021; Watters et al., 2021). Since the majority of processes driving deep convective diurnal variability, e.g. convection, radiation, cloud microphysics, turbulence, have to be parameterized in current Earth System Models (ESMs), it is not surprising that the simulated diurnal cycle of ESMs exhibits diurnal phase biases with a peak that typically occurs several hours too early (Christopoulos and Schneider, 2021). These phase biases of tropical convective processes in models

https://doi.org/10.5194/egusphere-2026-3869
Preprint. Discussion started: 31 July 2026

have been investigated by comparing observed and simulated surface precipitation, since high-frequent satellite or ground observations of precipitation are available (e.g. Yang and Slingo, 2001; Dai, 2006; Christopoulos and Schneider, 2021; Dai, 2023). Likewise, precipitation observations revealed considerable differences of diurnal cycles over tropical land and ocean areas (Dai, 2006; Christopoulos and Schneider, 2021). Over tropical land the precipitation diurnal cycle tends to have a larger amplitude compared to the ocean, and the diurnal maximum tends to occur in the late afternoon or early evening (Christopoulos and Schneider, 2021). In contrast, the precipitation diurnal cycle over the tropical ocean is typically less pronounced and the diurnal peak often occurs during the second half of the night or the early morning (Christopoulos and Schneider, 2021; Watters et al., 2021). However, Wessinger et al. (2025) recently found that the morphology of the tropical precipitation diurnal cycle over oceans is more complex and oceanic deep convective clouds with cloud tops warmer than 210 K in infrared brightness temperature tend to form a secondary diurnal precipitation peak during the afternoon.

Since most studies focused solely on characterizing the precipitation diurnal cycle, we will put the focus on investigating the diurnal cycles of frozen particles in this manuscript and complement the existing knowledge from precipitation-only analyses. So far, ice water concentration and the related ice water path have been sparsely used to investigate tropical diurnal cycles of deep convection. Eriksson et al. (2010) found a strong land-ocean contrast in the diurnal phase and amplitude of upper tropospheric ice water concentration and relative humidity in selected regions when combining two satellite datasets providing together four diurnal samples. Ocean regions have a diurnal ice water concentration peak in the early morning, while land areas have a distinct afternoon or early evening peak. Gong et al. (2018) found a strong diurnal cycle in ice particles and their micro-physical structure over tropical land but a negligible one over tropical ocean. Tian et al. (2020) investigated over the Great Plains that the peak of observed ice water path within mesoscale convective systems is synchronized with the diurnal cycle of precipitation within the convective core and stratiform precipitation area of the system. Here, we will complement these sparse or regional analyses with a diurnal cycle analysis of the quasi-global and half-hourly frozen water estimates of the Chalmers Cloud Ice Climatology (CCIC) satellite dataset (Amell et al., 2024). To our knowledge, CCIC is the first datasets that enables a quasi-global analysis of the full diurnal cycle of frozen water, while previous quasi-global satellite products allowed mostly daytime analyses.

In addition to single variable diurnal cycle analyses, Dai (2023) compared multiple convection-related variables from the ERA5 reanalysis and a diverse set of ground-based and satellite datasets. Key results of Dai (2023) with focus on deep convection processes are, that the IMERG precipitation product (Table 1) mainly captures the diurnal cycle of deep convection and that the average diurnal amplitude of high cloud cover over land and ocean is comparably small in contrast to that of low cloud cover. On average, ERA5 overestimates the precipitation diurnal cycle over tropical land areas while showing a similar diurnal amplitude over tropical land areas in total cloud cover (Dai, 2023). Such a multi-variable diurnal cycle analysis allows to connect the diurnal cycles of individual variables to obtain a more process-oriented diurnal cycle analysis. In the following we will use frozen water path, precipitation and high cloud cover to analyze the diurnal cycle of deep convection in the tropics.

In recent years, the class of km-scale models (e.g. Stevens et al., 2019) became computationally feasible allowing to simulate more realistic diurnal cycles with smaller phase biases compared to ESMs. Km-scale models, that directly simulate the bulk of deep convective processes without relying on a convection parameterization, and ESMs with nested 2D km-scale models have

https://doi.org/10.5194/egusphere-2026-3869
Preprint. Discussion started: 31 July 2026

in general smaller diurnal phase biases of precipitation than coarse-resolution ESMs (Song et al., 2024; Behrens et al., 2025). In addition, km-scale models capture causal relationships between precipitation, small-scale updraft statistics and large-scale column relative humidity (Ricard et al., 2025). Despite these advantages, km-scale models tend to overestimate the diurnal amplitude of summertime precipitation compared to satellite observations over land, showing in this particular case weaker skill than ESMs (Song et al., 2024). Recently, In and Khairoutdinov (2026) evaluated km-scale models including a brief diurnal cycle analysis for 200 hPa ice water and precipitable water compared to ERA5. Although ERA5 has a considerable underestimation of frozen particles compared to long-term satellite observations (e.g. CCIC) and thus is not the best baseline for the evaluation of frozen water in km-scale models (Eriksson et al., 2026; Pfreundschuh et al., 2025).

Previous work and the previously reported underestimation of frozen particles in ERA5 motivate us to have a closer look at the multivariate diurnal cycle of deep convection and evaluate biases of ERA5. In addition, we will compare the performance of km-scale models for frozen water path and precipitation against CCIC and IMERG.

This manuscript is structured as follows. Section 2 describes the data and methods to analyse the diurnal cycle of convective processes. It is followed by section 3 that describes zonal averages of frozen water path and precipitation from satellite observations, ERA5 and km-scale models. Section 4 investigates the entire diurnal cycle of frozen water path between 60° S and 60° N using CCIC, which was not possible with other satellite products to our knowledge. Then, we compare the diurnal cycle of precipitation and high cloud cover together with frozen water path in six tropical and subtropical regions. We conclude this section with an evaluation of the simulated regional diurnal cycles of frozen water path and precipitation in km-scale models that participated in the DYAMOND winter project (Stevens et al., 2019) against CCIC and IMERG. Section 5 discusses the key differences of the observed and simulated diurnal cycles. It further assesses similarities of the satellite-observed diurnal cycles of frozen water path, precipitation and high cloud cover, to obtain a better understanding of the diurnal cycle of deep convective processes. This manuscript concludes with section 6 that summarizes key findings of the diurnal cycle analysis of deep convective processes in the tropics.

2 Data and methods

This section briefly introduces the two observational products: the Chalmers Cloud Ice Climatology (CCIC, Table 1, Amell et al., 2024) for frozen water path (FWP, the integral over all suspended and precipitating ice particles in the atmospheric column, e.g. Waliser et al., 2009) and high cloud cover (HCC, cloud fraction of all cells above 6 km altitude) and the Global Precipitation Measurement Integrated Multi-satellite Retrievals for GPM version 7 (IMERG, Table 1, Huffman et al., 2023b) for precipitation. Afterwards, we briefly describe the two reference datasets: ERA5 (Hersbach et al., 2020) and DYAMOND (Stevens et al., 2019), and the preprocessing and diurnal cycle analysis steps.

Table 1 gives an overview of all the datasets and methods used in this manuscript and introduces acronyms that will be used in the following.

https://doi.org/10.5194/egusphere-2026-3869
Preprint. Discussion started: 31 July 2026

2.1 Observational Datasets

2.1.1 Chalmers Cloud Ice Climatology (CCIC)

CCIC (Table 1, Amell et al., 2024) is a machine-learning (ML) based cloud ice product created from satellite observations. Here we use the half-hourly version of CCIC, which is based on the Climate Prediction Center globally merged IR product version 1 (CPCIR, e.g. Janowiak et al., 2001). The ML algorithm of CCIC uses the CPCIR brightness temperatures at 11 μm and infers FWP, ice water content, a 2D cloud and a 3D cloud probability. The CloudSat and CALIPSO ice cloud property version R05 level2 data (2C-ICE, e.g. Deng et al., 2015) and the cloud scenario classification version R05 level 2 data (2B-CLDCLASS-LIDAR, Sassen and Wang, 2008) serve as training data for the ML algorithm. CCIC has a horizontal resolution of 0.036° like CPCIR and a temporal resolution of 0.5 hours. For a detailed explanation of the training data and the respective optimization of the ML algorithm we refer to Amell et al. (2024). Amell et al. (2024) and Pfreundschuh et al. (2025) compared CCIC against existing satellite products and data from field campaigns. Here, we focus on deep convective processes in the tropics that are well captured in the CCIC's variables FWP and high cloud cover (HCC, Table 1, the latter extracted from its 3D cloud mask estimates from an altitude of >= 6 km above ground.). FWP of CCIC is used for the period 2018-2023 (Table 1), while we analyse HCC for the year 2018. We select these periods to exclude major El Niño–Southern Oscillation events and to coincide with the km-scale model data from DYAMOND.

2.1.2 Global Precipitation Measurement Integrated Multi-satellitE Retrievals for GPM

For the precipitation (precip, Table 1) we use the Global Precipitation Measurement Integrated Multi-satellitE Retrievals for GPM version 7 final (IMERG, Table 1, Huffman et al., 2023b). This dataset is based on a combination of satellite measurements including, e.g. passive microwave and infrared data from the global precipitation measurement constellation (Pfreundschuh et al., 2024) and ground-based rain gauge measurements and precipitation radar data for calibration (Huffman et al., 2023b). For more information on GPM, we refer to e.g. Huffman et al. (2023b); Pfreundschuh et al. (2024). We use the identical time period (year 2018 - 2023) for IMERG, see Table 1. IMERG in the final gridded version has a horizontal resolution of 0.1° and a temporal resolution of 0.5 hours. We are aware of the potential sub-diurnal oscillations in IMERG, due to the data assimilation process of microwave measurements (Amell et al., 2025; Yuval et al., 2026). However, we do not notice any clear effects of this in our diurnal cycle analysis that would require a low-pass filtering of IMERG as Yuval et al. (2026) suggested for their diurnal cycle analysis.

2.2 Evaluated Datasets

2.2.1 ERA5

We use the European Centres for Medium-Range Weather Forecasts (ECMWF)'s fifth generation reanalysis (ERA5, Hersbach et al., 2020) as an evaluated dataset for our diurnal analysis. ERA5 is based on a multitude of different Earth observations. These are used as boundary and initial conditions of ECMWF's integrated forecasting system (IFS) cycle Cy41r2 that builds

https://doi.org/10.5194/egusphere-2026-3869
Preprint. Discussion started: 31 July 2026

Dataset	Variables	Type	Period	Δx	Δt	Preprocess. steps
CCIC (Amell et al., 2024)	FWP, HCC	Obs.	2018 - 2023 for FWP, 2018 for HCC	0.036°	0.5 h	regridding to 1°, averaging to 1 h
IMERG (Huffman et al., 2023b)	precip	Obs.	2018 - 2023	0.1°	0.5 h	regridding to 1°, averaging to 1 h
ERA5 (Hersbach et al., 2020)	FWP, precip, HCC	Reanalysis	2018 - 2023, 2018 for HCC	0.25°	1 h	regridding to 1°
DYAMOND (Stevens et al., 2019)	FWP, precip[a]	km-scale models	February 2020	O(5km)	0.5 h	regridding to 1°, averaging to 1 h [b]

[a]different precip variables were stored and preprocessed, see Table S1
[b]in addition unit conversions for precip were necessary for individual DYAMOND members see Table S1

Table 1. Overview of the used datasets to analyse the diurnal cycles of frozen water path (FWP), precipitation (precip) and high cloud cover (HCC). The table displays the acronyms of the used datasets, the variables, the type of the dataset, the respective time period, the horizontal and temporal resolution and preprocessing steps applied.

the numerical backbone of ERA5 (see Hersbach et al. (2020) for more information). Here, we assess whether ERA5 has deficiencies in capturing the diurnal cycle of deep convection compared to satellite observations, considering that it relies e.g. on the mass-flux convection parameterization of IFS to simulate convective processes during its data generation. For ERA5 we estimate FWP via summing up total large-scale snow and ice water paths following Pfreundschuh et al. (2025). However these estimates do not include the amount of frozen hydrometeors (e.g. graupel) from the convection scheme of IFS, which are not available in the ERA5 dataset. This results in a general underestimation of FWP of ERA5 compared to satellite observations (Pfreundschuh et al., 2025; Eriksson et al., 2026). In addition to the FWP estimates from ERA5, we use precip in the period from 2018 to 2023 and HCC for 2018 from the reanalyis product (Table 1). ERA5 has the coarsest horizontal resolution with 0.25° and temporal resolution with 1 hour of all used datasets (Table 1). CCIC and ERA5 have a similar “definition” of HCC and a previous study found negligible deviations in HCC due to the different vertical axes (Amell et al., 2026). Consequently, we assume that HCC of CCIC and ERA5 are directly comparable with each other.

2.2.2 DYAMOND simulations

As a second evaluated dataset we use the orchestrated DYnamics of the Atmospheric General Circulation Modeled on Non-Hydrostatic Domains (DYAMOND, Stevens et al., 2019) winter simulations of several km-scale models (also known as storm-resolving or cloud resolving models in literature). The participating modeling groups performed (quasi)-global simulations on km-scale (5 km and finer) that span the time period from 20^{th} January 2020 through the end of February 2020. For our diurnal cycle analysis we use data from February 2020. We use FWP from 9 participating models, precip is available from 5 models. For more details about individual km-scale models and necessary preprocessing steps we refer to Table S1 in the supplement.

https://doi.org/10.5194/egusphere-2026-3869
Preprint. Discussion started: 31 July 2026

2.3 Methods

To compare CCIC, ERA5 and DYAMOND we regrid all datasets to a regular 1° x 1° latitude-longitude grid with a first-order conservative regridding algorithm using the Climate Data Operators (Schulzweida, 2023). We further compute hourly averages of the variables of interest from CCIC and the DYAMOND models to have the same temporal resolution as ERA5. We restrict our analysis to the latitude range of CCIC between 60 °S and 60 °N. Next, for all datasets, we average the time series into a composite 24-h day for each month in the study period. This enables easier data handling when further averaging over selected regions and over the study period in Section 4 and when calculating the diurnal amplitude and peak time in global latitude-longitude maps, which is described in the following.

2.3.1 Diurnal cycle analysis

Two standard metrics to describe a diurnal cycle are its amplitude and its peak time (Covey et al., 2016; Dai, 2023; Watters et al., 2021). To compute amplitudes and peak times of a variable F, we perform a harmonic decomposition in each grid cell, that can be described with Equation 1:

$$F(t) = M_0 + S_1 \sin\left(\frac{2\pi t}{24}\right) + C_1 \cos\left(\frac{2\pi t}{24}\right) + S_2 \sin\left(\frac{2\pi t}{12}\right) + C_2 \cos\left(\frac{2\pi t}{12}\right). \quad (1)$$

where t is the time of day (local solar time) in hours, M_0 is the mean, S_1 and C_1 are the diurnal coefficients and S_2 and C_2 are the semi-diurnal coefficients. The right-hand-side of the equation is then fitted to $F(t)$ using least squares. High-frequency components above the 12-hour and 24-hour mode are not providing additional information for FWP, precip and HCC in our case in agreement with previous literature (Watters and Battaglia, 2019).

The amplitude of the diurnal cycle A, is defined as the difference between the minimum and the maximum of the fitted curve $F(t)$:

$$A = \max[F(t)] - \min[F(t)]. \quad (2)$$

The peak time t_{peak} of the diurnal cycle is defined as the time when $F(t)$ reaches its maximum:

$$t_{peak} = \text{argmax}_{t\in[0,24)} F(t). \quad (3)$$

We are not distinguishing between 24-hour or 12-hour components for their contributions to amplitude or peak time in the following. For FWP, we found that the 24-hour mode explains most of the diurnal variability, whereas the 12-hour component improves the fit (Leko, 2025). We convert the time from UTC to local solar time (LST) in each grid cell with Equation 4:

$$\text{LST} = \text{UTC} + \frac{\text{lon}}{15°h^{-1}}, \ \text{lon} \in [-180, 180]. \quad (4)$$

https://doi.org/10.5194/egusphere-2026-3869
Preprint. Discussion started: 31 July 2026

2.3.2 Masking in peak time maps

In regions where the diurnal cycle amplitude is small or where the quality of the fit is poor (see our criterion on diurnal amplitude and fit quality below), it is challenging to define a robust peak time. Consequently, these areas need to be masked in the peak time maps. Several approaches have been developed for masking precip peak times. For example, Covey et al. (2016) use a lower and a upper threshold of relative amplitudes (amplitude divided by its mean), in addition to a monthly mean precipitation threshold that identifies dry regions, where precipitation is sporadic. However, this approach is not working well for FWP. Alternatively, Jeong et al. (2011) and Watters and Battaglia (2019) use explained variance (R^2) for thresholding, which describes how well the fitted function in Eq. 1 describes the data (Equation 5):

$$R^2 = 1 - \frac{\text{RSS}}{\text{TSS}}. \tag{5}$$

The residual sum of squares (RSS) and the total sum of squares (TSS), are defined as:

$$\text{RSS} = \sum_{i=1}^{n} (y_i - \hat{y}_i)^2, \tag{6}$$

$$\text{TSS} = \sum_{i=1}^{n} (y_i - \bar{y})^2, \tag{7}$$

where y_i are observed data values, $\hat{y}_i$ are the fitted values, and $\bar{y}$ is the mean of the observed values. The closer R^2 is to the value of 1, the better the fit explains the variance in the data.

For FWP we find as the best masking method, when grid cells are excluded from the diurnal analysis of peak time that meet at least one of these requirements:

1) The climatological mean FWP of the grid cell is less than the 25^{th} percentile of the global FWP field.

2) R^2 is less than 0.6.

We use the same method for the masking of precip and HCC.

2.3.3 Peak time statistics

In order to make our diurnal analysis more accessible and quantitative, basic statistics of the diurnal peak time and diurnal cycle's amplitude in CCIC FWP are computed and displayed in Table 2. This includes the mean (weighted with latitude), the 10^{th} percentile and the 90^{th} percentile as variability estimates. Since the peak time is a circular variable, it needs to be converted from hours to radians to compute its statistics. For the mean, the mean of respective cosines and sines in Equation 1 is calculated. The respective percentiles are calculated after re-centering around the calculated mean, and converting them back to hours in LST.

https://doi.org/10.5194/egusphere-2026-3869
Preprint. Discussion started: 31 July 2026

3 Zonal mean analysis

In the following, we analyse the zonal means of FWP and precip for the summer (JJA) and winter season (DJF) in the period 2018 - 2019 and for February 2020. We use the shorter time period 2018 - 2019 to allow a direct comparison between CCIC and the FWP from the DARDAR (Delanoë and Hogan, 2010) and 2C-ICE products. This analysis compares FWP and precip from observations, ERA5 and km-scale models.

Figure 1a shows the zonal means of FWP of CCIC and ERA5 for JJA and DJF averaged over the period 2018 to 2019. Figure 1b displays the zonal averages of FWP from CCIC, ERA5 and km-scale models in February 2020. Figure 1c,d shows the respective zonally averaged precip from IMERG, ERA5 and the km-scale models.

For FWP there exists a known uncertainty in retrieved zonal averages of about 20% between different products based on CloudSat / CALIPSO data (Eriksson et al., 2026). To account for this uncertainty in traditional FWP retrievals we include the 2C-ICE (upper bound) and DARDAR estimates (lower bound) in Fig. 1a, as a conservative representation of this uncertainty.

Figure 1a shows that the FWP in CCIC is on average about twice as large as in ERA5, independent of the season, due to the missing convectively formed frozen hydrometeors. The same can also be seen when comparing ERA5 with 2C-ICE or DARDAR, for the latter the deviations are less pronounced (around 0.1 $\mathrm{kg\,m^{-2}}$ in the tropics). Convectively formed frozen hydrometeors have a higher contribution to the total FWP in the tropics due to the frequent deep convection within the inter-tropical convergence zone (ITCZ), see Pfreundschuh et al. (2025) for a detailed analysis. This missing component in the FWP values from ERA5 has to be taken into consideration when evaluating both basic zonal statistics and the diurnal cycle (e.g. by calculating relative diurnal amplitudes for FWP to enable an easier visual comparison between CCIC and ERA5 like in Leko, 2025).

Despite this large underestimation of more than -0.15 $\mathrm{kg\,m^{-2}}$ in the tropics, ERA5 is capable of reproducing the seasonal shifts in FWP that are observed in CCIC. In detail, the respective austral or boreal mid latitudes have a considerably higher FWP during their respective winter season than during their respective summer seasons. Likewise the migration of the ITCZ from 10 °S during winter to 5 °N in summer is well captured in ERA5. The zonal averages of CCIC and ERA5 also correlate well in February 2020 (see Fig. 1b), conditioned on the FWP underestimation in ERA5. The multi-model mean FWP of the DYAMOND models aligns well with CCIC in the tropics as reported by Eriksson et al. (2026). The multi-model mean of DYAMOND has a higher mean FWP within the tropics than ERA5, reducing the difference to CCIC to around -0.07 $\mathrm{kg\,m^{-2}}$ in the tropics. However this comes at the expense of an elevated ensemble spread (= measured between the minimum and maximum member of zonally averaged FWP of all analysed DYAMOND models) in the proximity of the first and second FWP peak in the tropics. This ensemble spread is 1.5 times larger than the mean FWP of the DYAMOND models at 10 °S. A comparably large ensemble spread of the DYAMOND models of maximum 0.4 $\mathrm{kg\,m^{-2}}$ in the tropics can be seen in the ocean-only analysis of Ćorko et al. (2025) in the DYAMOND "summer" experiments (Stevens et al., 2019). Here, in the DYAMOND winter simulations the ensemble further shows a general underestimation of FWP in the boreal mid latitudes during February 2020 compared to CCIC and ERA5. Similarly, FWP from DYAMOND models is also underestimated in the mid latitude storm track regions in summer compared to 2C-ICE (Ćorko et al., 2025).

https://doi.org/10.5194/egusphere-2026-3869
Preprint. Discussion started: 31 July 2026

For precip, the zonal averages of IMERG and ERA5 agree considerably well in the tropics in the period 2018 to 2023 throughout all seasons (Fig. 1c). The seasonal shift of the ITCZ in precip is well captured in ERA5, too, though ERA5 exhibits a small moist bias of up to 0.03 $\mathrm{mm\,h^{-1}}$ compared to IMERG in all seasons. In the extratropics the zonally-averaged precip from IMERG and ERA5 has a difference of around 0.03 $\mathrm{mm\,h^{-1}}$. ERA5 has in all seasons a too poleward extending representation of the austral or boreal storm track regions in precip compared to IMERG. These south or northward extending storm track regions in ERA5 are also visible in February 2020. In the tropics ERA5 and IMERG agree well in February 2020 with a small moist bias of ERA5 compared to to IMERG of up to of around 0.03 $\mathrm{mm\,h^{-1}}$. The analysed DYAMOND models show typically larger deviations to IMERG (up to 0.08 $\mathrm{mm\,h^{-1}}$ at 5 °N) than ERA5 and have also a considerably large spread of more than 0.1 $\mathrm{mm\,h^{-1}}$ near the peak in the zonally averaged distribution at 10 °S. Moreover DYAMOND models show a too strong secondary precip peak in February 2020 north of the Equator at 5 °N. This secondary peak exceeds on average the southern hemispheric first precip peak at 10 °S related to the ITCZ (Fig. 1d). Figure 1d in combination with our diurnal cycle analysis of precip (Figs. 8,S2,S8) may question the ability of the DYAMOND models to represent boreal wintertime precipitation patterns (e.g. the ITCZ and South Pacific Convergence Zone (SPCZ)) in the tropics in agreement with the findings of In and Khairoutdinov (2026). Thus we will focus mainly on the ensemble mean of all DYAMOND models in FWP and precip and compute averages in 6 regions (see boxes in Fig. 4b) in the tropics to compare against observations and ERA5.

For ERA5 we will perform a detailed investigation of the diurnal cycle's amplitude and the respective peak time compared to CCIC and IMERG in latitude-longtitude maps in the next section.

4 Diurnal Cycle Analysis

In this section, we will first have a look at the full diurnal cycle of FWP on a quasi-global scale (60 °S - 60 °N) which is to our knowledge only possible with CCIC from a satellite perspective. Then we will focus on six selected tropical regions based on Eriksson et al. (2014). In these six regions, we will analyse the diurnal cycles of FWP, precip and HCC from observations, and compare ERA5 and the DYAMOND km-scale models against CCIC.

4.1 Frozen Water Path

To start the diurnal cycle analysis we will look at the diurnal amplitude and the diurnal peak of FWP, and some general diurnal statistics in CCIC for the period 2018 - 2023. Figure 2 shows maps of the diurnal cycle amplitude for FWP from CCIC and the corresponding difference to ERA5 (ERA5 - CCIC) for the winter (DJF), spring (MAM), summer (JJA) and fall (SON) season. It is accompanied by Fig. 3 that shows the diurnal peak time of FWP in all seasons. To complement the analysis we include Table 2 that displays general statistics of the FWP diurnal cycle in the tropics and boreal mid latitudes in CCIC.

The amplitude of the diurnal cycle of FWP is clearly influenced by deep convection in the tropics, orography and seasonal variability (Fig. 2, Table 2). In the tropics we see the largest diurnal cycle amplitudes of FWP along the ITCZ, the SPCZ and over tropical South America and Africa with values exceeding 0.3 $\mathrm{kg\,m^{-2}}$ throughout the seasons associated with frequent deep convection in these regions. In contrast, there is a negligible diurnal cycle over the upwelling regions offshore of Peru

https://doi.org/10.5194/egusphere-2026-3869
Preprint. Discussion started: 31 July 2026

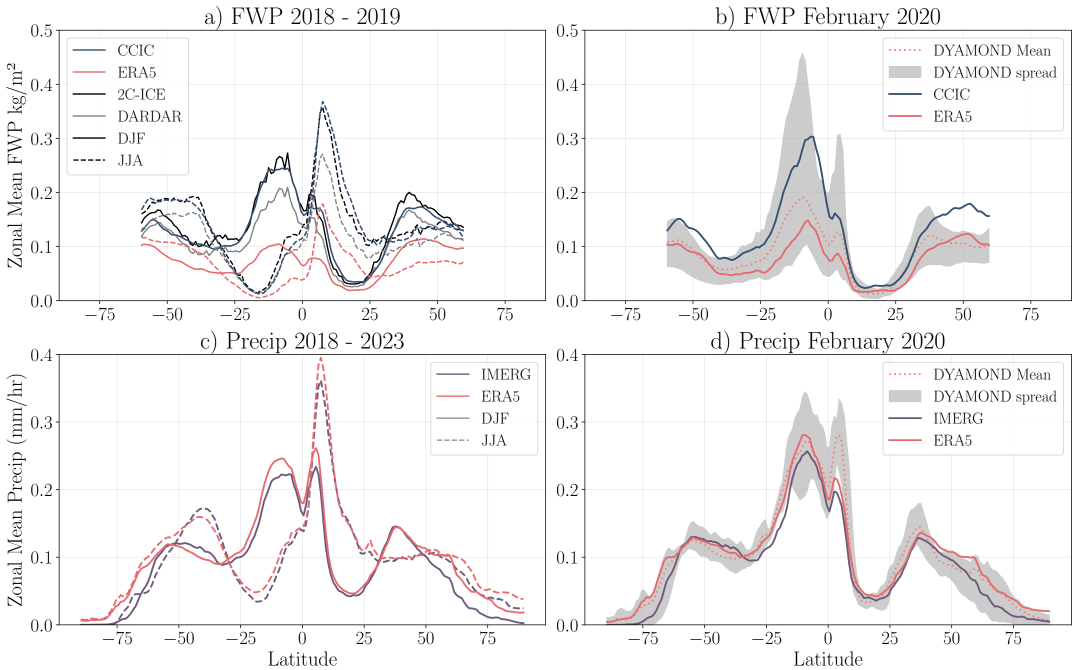

Figure 1. a) Zonal averages of frozen water path (FWP) in CCIC (blue), ERA5 (red), 2C-ICE (black) and DARDAR (gray) during boreal winter (solid, DJF) and boreal summer (dashed, JJA) averaged over the period 2018 to 2019. b) zonal averages of FWP of CCIC (dashed blue), ERA5 (solid red) and the DYAMOND multi-model mean (dotted orange curve) in February 2020. c) Zonal averages of precipitation (precip) in IMERG (purple), ERA5 (red), during boreal winter (solid, DJF) and boreal summer (dashed, JJA) averaged over the period 2018 to 2023. d) zonal averages of precip of IMERG (solid purple), ERA5 (solid red) and the DYAMOND multi-model mean (dotted orange curve) in February 2020. The range between minimum and maximum of all DYAMOND models in zonally-averaged precip is indicated by the gray area.

and Angola due to the stable atmospheric conditions that generally inhibit deep convection. CCIC further captures two distinct seasonal features of FWP. First, an elevated diurnal amplitude of FWP over the boreal mid-latitude land area during summertime and reduced amplitudes during wintertime (Fig. 2, Table 2). Second, an increased diurnal amplitude of FWP during the summertime over India and adjacent Southeast Asia and a reduced diurnal amplitude during wintertime over these regions, which is well aligned with the driving monsoon circulation. Similar but less pronounced characteristics of monsoon circulations in the diurnal amplitude maps of CCIC are visible over West Africa, around Madagascar, northern parts of Australia and Northeastern Mexico.

All these regions, except the tropical upwelling regions, illustrate clear differences between CCIC and ERA5 (Fig. 2b). Similarly to the underestimation of the zonal means of FWP in the tropics (Fig. 1), we see a generally too weak diurnal amplitude along the ITCZ and during the respective monsoon seasons over affected areas (e.g. India, West Africa) in ERA5. The bias in FWP amplitudes exceeds -0.1 $\mathrm{kg\,m^{-2}}$ over tropical land areas like the Amazonas region or the Congo basin.

https://doi.org/10.5194/egusphere-2026-3869
Preprint. Discussion started: 31 July 2026

Likewise, ERA5 underestimates the diurnal amplitude of FWP by around 0.1 $\mathrm{kg\,m^{-2}}$ over boreal mid latitude land areas during summer. A weak positive bias, with a 0.01 $\mathrm{kg\,m^{-2}}$ higher diurnal FWP amplitude in ERA5, exists at the southern edge of the ITCZ over the equatorial Pacific throughout all seasons. This may be related to a slightly more southern ITCZ location in ERA5 (seen also between IMERG and ERA5 in Fig. S2b) compared to CCIC and IMERG.

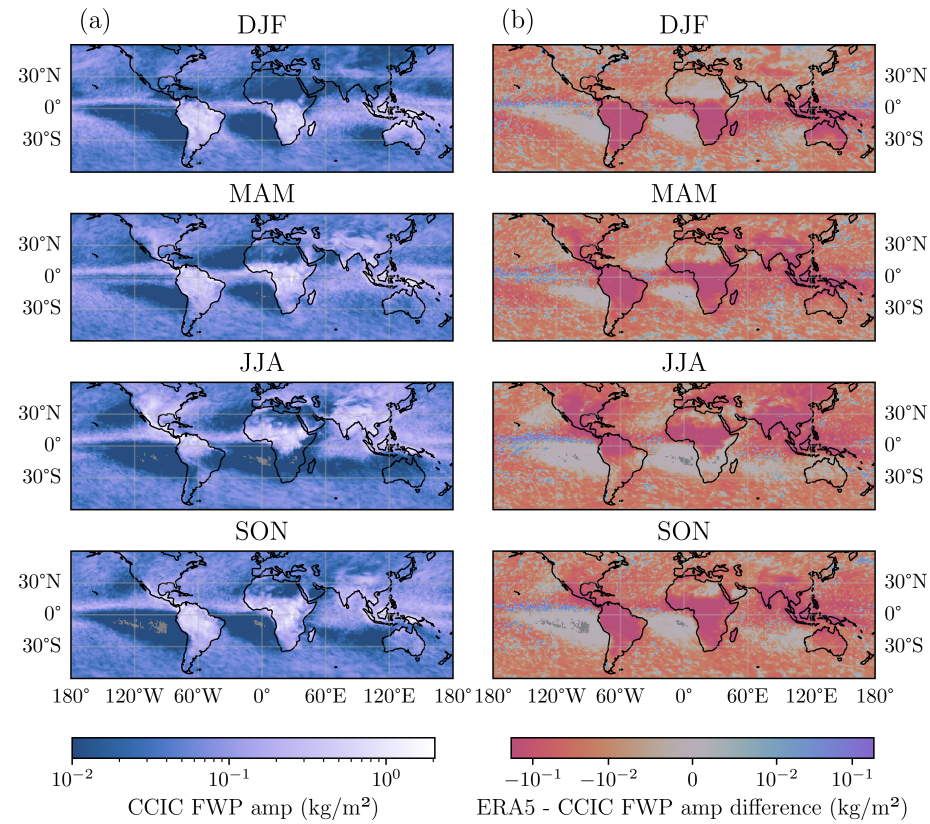

Figure 2. Diurnal amplitude of FWP in CCIC for the four seasons: December-January-February (DJF), March-April-May (MAM), June-July-August (JJA) and September-October-November (SON), averaged over the period 2018 - 2023 in panel (a) and differences compared to ERA5 in panel (b). The gray areas indicate missing values.

Compared to the diurnal amplitude, the diurnal peak time of FWP in CCIC exhibits a large spatial heterogeneity, especially over mid-latitude ocean areas (Fig. 3a). However, we see more clearer and more homogeneous patterns in the tropics and over the boreal mid-latitude land areas during the summer. In CCIC tropical land masses' peak times are predominated by late afternoon or early evening peaks (16 - 19 LST, Fig. 3a, Tab. 2), while in the maritime ITCZ regions peak times are predominated by nighttime or early-morning peaks (0 - 9 LST, 3a, Tab. 2). In the tropics, e.g. the Andes, the Venezuelan highlands or the highlands of southern Congo in CCIC's FWP stand out with a tendency towards a diurnal peak during nighttime around 0 LST in CCIC. CCIC captures the well-known nighttime eastward propagation of deep convective cells over the Central US (e.g.

https://doi.org/10.5194/egusphere-2026-3869
Preprint. Discussion started: 31 July 2026

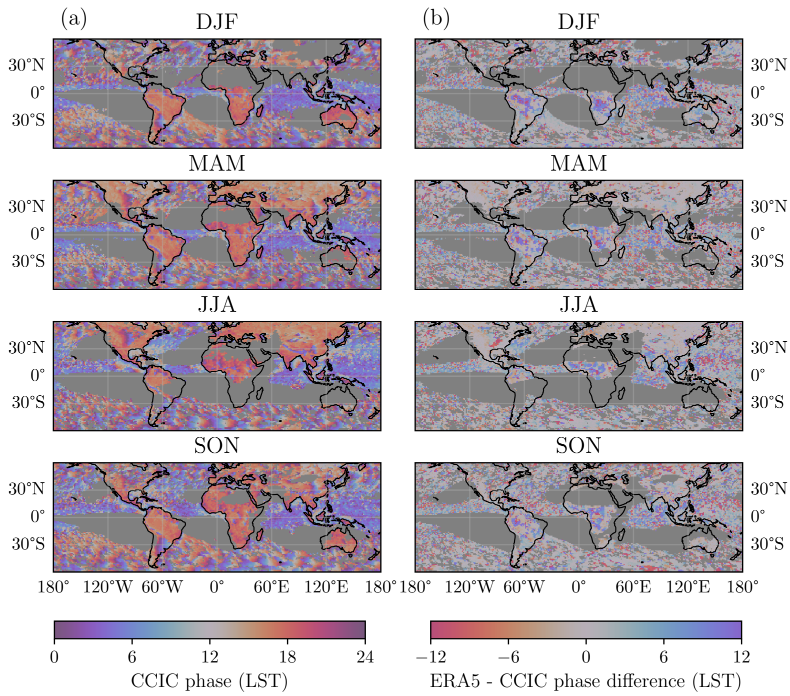

Figure 3. Diurnal peak time of FWP in CCIC for the four seasons averaged over the period 2018 - 2023 in panel (a) and differences compared to ERA5 in panel (b). The masked areas (dark gray) have negligible FWP or diurnal variability (see Section 2.3.2).

	CCIC FWP diurnal amplitude [$\frac{kg}{m^2}$]			CCIC FWP peak time (LST) [a]		
period 2018 - 2023	mean	10^{th} perc.	90^{th} perc.	mean	10^{th} perc.	90^{th} perc.
Tropics ocean	0.092	0.007	0.183	06:00	00:00	16:00
Tropics land[b]	0.308	0.082	0.545	18:00	15:00	02:00
boreal mid. lat. land DJF	0.034	0.012	0.059	14:00	06:00	23:00
boreal mid. lat. land JJA	0.122	0.042	0.220	16:00	14:00	21:00

[a] rounded to the next full hour
[b] We excluded arid areas (e.g. the southern part of the Sahara desert) with a mean FWP below 0.037 kg m^{-2} here

Table 2. Statistics of the diurnal cycle from CCIC's FWP for the period 2018 - 2023. This table shows the mean, the 10^{th} percentile and 90^{th} percentile of the diurnal cycle amplitude (2^{nd} column) and the mean, extreme percentiles of the peak times (3^{rd} column). We show the general statistics for the tropical (20 °S - 20 °N) ocean and land area, and the boreal mid latitude land area (35 °N - 60 °N) during winter (DJF) and summertime (JJA).

Watters et al., 2021) during spring and summer (Fig. 3a). The bias of reanalysed FWP peak time of ERA5 compared to CCIC are in most grid cells within ±6 hours. Especially the biases of ERA5 in FWP during summer over the boreal mid latitudes land area and CCIC is within ±1 hour. A diurnal bias with a 4 to 5 hour too early peak in FWP in ERA5 is visible over the

https://doi.org/10.5194/egusphere-2026-3869
Preprint. Discussion started: 31 July 2026

southern Mississippi area, which is in agreement with e.g. the investigated bias in precip of Watters et al. (2021). Our own IMERG diurnal analysis, however, indicates a tendency of ERA5 to trail behind by 2 to 5 hours on grid scales in our shorter analysis period from 2018 - 2023 over this region (Fig. S3).

The largest diurnal biases between CCIC and ERA5 in FWP diurnal peak time can be seen in maps over Amazonia and the Congo basin (Fig. 3). Here, the FWP peak time differs locally by more than ± 10 hours. As a result of that, we will have a closer look on the full diurnal cycle in these regions, see Fig. 4b and the box "Africa" $[20^\circ\,\mathrm{S} - 5^\circ\,\mathrm{N}, 15^\circ\,\mathrm{E} - 35^\circ\,\mathrm{E}]$ including the Congo basin and the box "South America" $[15^\circ\,\mathrm{S}\ - 0^\circ\,\mathrm{N}, 75^\circ\,\mathrm{W} - 40^\circ\,\mathrm{W}]$ over Amazonia. The definition of these regions and 4 other that are introduced in the following is based on a previous analysis from Eriksson et al. (2010, 2014). A similar large uncertainty of around ± 8 hours in the peak time of FWP between CCIC and ERA5 is visible over the central tropical Indian Ocean south of the Equator, which is contained in the "Tropical Indian" box $[20^\circ\,\mathrm{S} - 0^\circ\,\mathrm{N},\ 55^\circ\,\mathrm{E} - 90^\circ\,\mathrm{E}]$. A difference of around ± 6 hours hours between ERA and CCIC is also present east of Australia in the SPCZ (Fig. 3), which is contained in the "Tropical Pacific" $[20^\circ\,\mathrm{S} - 0^\circ\,\mathrm{N}, 160^\circ\,\mathrm{E} - 160^\circ\,\mathrm{W}]$ box. Further we select the "Maritime Continent" $[10^\circ\,\mathrm{S} - 10^\circ\,\mathrm{N}, 100^\circ\,\mathrm{E} - 150^\circ\,\mathrm{E}]$ box due to the strong contrast between afternoon peaks over the Islands of Indonesia and the nighttime peaks over the surrounding ocean areas throughout all seasons (Fig. 3a) for our evaluation. For similar reasons, we use the "North Pacific" $[15^\circ\,\mathrm{N} - 30^\circ\,\mathrm{N}, 140^\circ\,\mathrm{E} - 160^\circ\,\mathrm{W}]$ box due to the difference of more than -0.05 $\mathrm{kg\ m^{-2}}$ in diurnal amplitudes between ERA5 and CCIC in FWP especially during the boreal summer (Fig. 2b).

Figure 4 shows the averaged diurnal cycle of FWP within the six tropical regions defined above for the period 2018 - 2023. In order to improve the comparability of the biases we normalise the diurnal cycles from ERA5 and CCIC reducing the effects of the general underestimation of FWP in ERA5 (Figs. 1,2). In the normalization step we divide the hourly values with the mean of the diurnal curve. Afterwards we compute the residuals between the values and the average of the normalized curve and display the results in percent.

The relative diurnal variations of CCIC are consistent with the ones reported by Eriksson et al. (2014), based on fully independent observations (limited to 6 months 2009-10); both the relative amplitudes and diurnal phases of CCIC agree well with the predecessing diurnal cycle analysis based on upper-tropospheric ice water content.

In detail, tropical land areas (Fig 4, Africa and South America) are characterized by a diurnal cycle with a higher relative amplitude in FWP compared to ocean areas or the Maritime continent for both CCIC and ERA5. This is in agreement with the large-scale statistics of the absolute FWP of CCIC in Table 2. Over the Maritime Continent we see good agreement between CCIC and ERA5 with negligible differences in phase and magnitude of the relative diurnal cycles. The CCIC and ERA5 curves show two peaks at 3 LST and 15 LST in all seasons. The first peak is associated with ocean grid cells while the afternoon peak is associated with land grid cells (Fig. 3a). Over the Tropical Pacific ERA5 FWP peaks too late by 2 hours at 8 LST in all seasons. ERA5 further shows an evening minimum, seen in CCIC at 18 LST, with a similar delay in all seasons. In the Tropical Indian box CCIC FWP shows a diurnal peak at around 4 LST in all seasons and a diurnal minimum around 18 LST. The ERA5 diurnal cycle of FWP has a different shape with a diurnal peak at around 13 LST. In the North Pacific the curves show the smallest diurnal amplitude which is in agreement with Eriksson et al. (2010, 2014). In CCIC the FWP diurnal cycle shows a bimodality with a morning peak at around 6 LST and second more pronounced one at around 17 LST in all seasons. ERA5

https://doi.org/10.5194/egusphere-2026-3869
Preprint. Discussion started: 31 July 2026

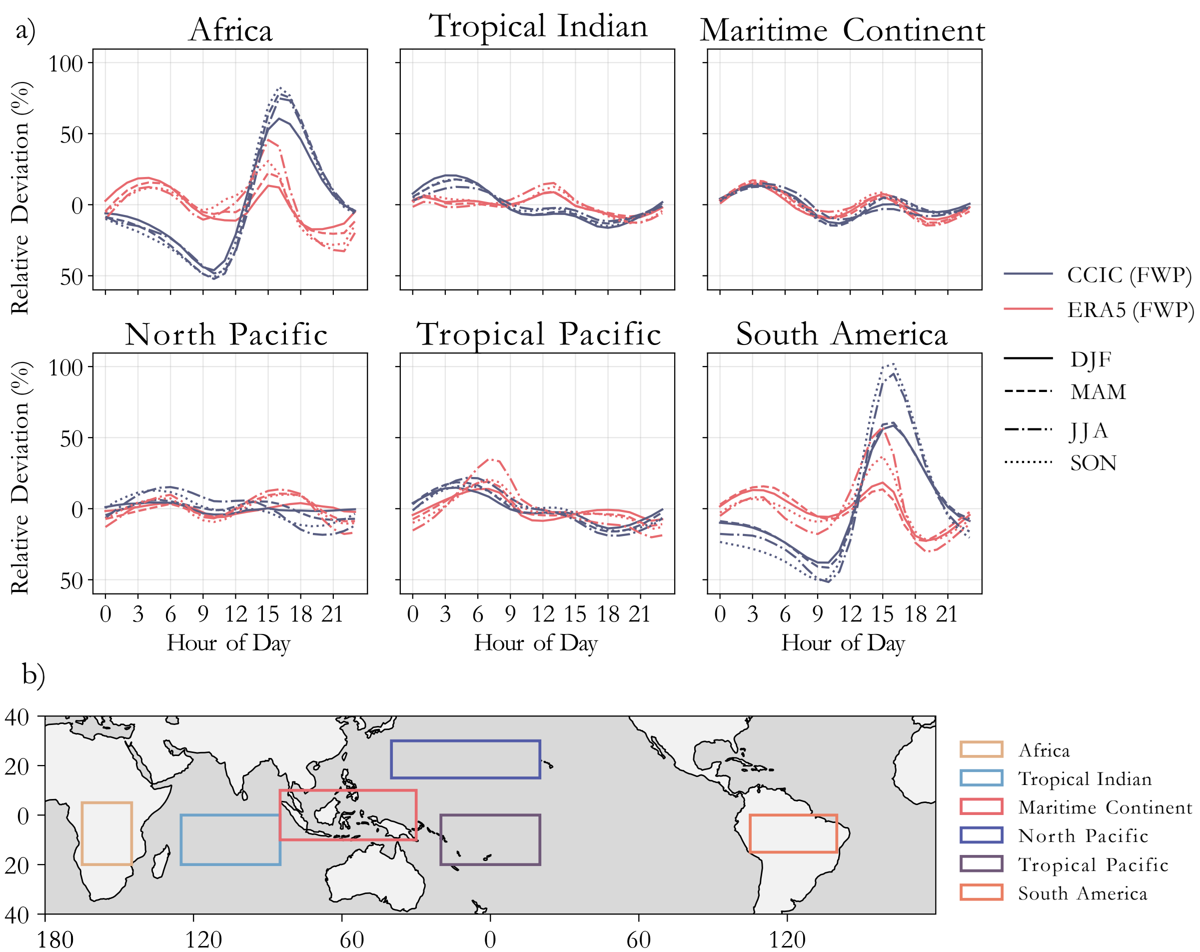

Figure 4. (a) Regional diurnal cycles of FWP in CCIC (blue) and ERA5 (red) over six regions. FWP is described in relative terms (as normalized deviation with respect to the respective diurnal mean) and shown for DJF (solid), MAM (dashed), JJA (dot-dashed) and SON (dotted) for 2018-2023. b) Definition of the six tropical regions: Africa (yellow), Tropical Indian (light blue), Maritime Continent (red), North Pacific (dark blue), Tropical Pacific (purple) and South America (orange).

captures the early morning peak but otherwise does not show the diurnal behavior from CCIC in the North Pacific. In Africa and South America the relative diurnal cycle of FWP in CCIC is influenced by seasonal variability. We see the largest amplitude of the relative diurnal cycle during the seasons with the weakest convection over these areas (for Africa: MAM, JJA and SON; for South America: JJA and SON, see Figs. 2,5,S2). In these two regions ERA5 shows a clear bimodality of the diurnal cycle of FWP, with a first peak at around 15 LST and a second one at around 4 LST independent of the season. In contrast, CCIC shows a pronounced unimodal diurnal cycle in FWP in the South America and Africa box. The diurnal peak in CCIC's FWP occurs in the Africa and South America box at 16 LST in all seasons and a minimum of FWP occurs at 10 LST. Closely inspecting the

https://doi.org/10.5194/egusphere-2026-3869
Preprint. Discussion started: 31 July 2026

respective latitude-longitude peak time maps in Figs. 3, S1 and the box-averaged diurnal cycle in Fig. 4 over the two tropical land areas, one explanation for the secondary peak of FWP in ERA5 at 4 LST is the larger regional extent of the nighttime deep convection along the Andes, the highlands of Venezuela and mountain ranges adjacent to the Congo basin towards low-lying neighboring areas in ERA5 compared to CCIC.

Compared to ERA5 we find that CCIC has typically a considerably stronger diurnal cycle over land in FWP. Especially over land areas we see a strong mismatch of the phase of the represented diurnal variability between the two datasets. To better understand this behavior in the Africa and South America box we compare the diurnal cycle of precip from ERA5 with IMERG and of HCC from CCIC next.

4.2 Regional analysis in the tropics: Precipitation and High Cloud Cover

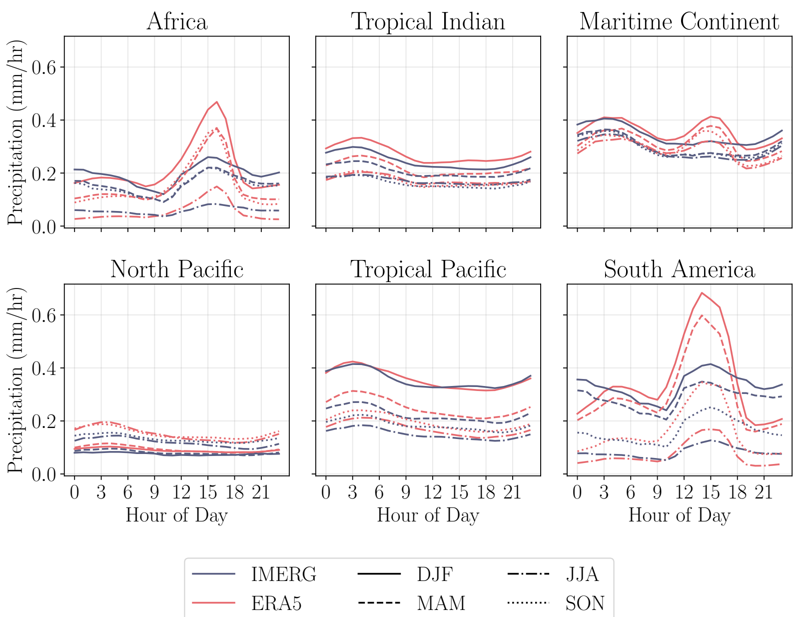

Figure 5. Regionally averaged diurnal cycles of the precipitation rate from IMERG (purple) and ERA5 (red), shown for the four seasons in the time period 2018-2023. The regions are defined in Fig. 4.

In the following, we analyse the diurnal cycle of precip. We would like to note that IMERG, used as the reference dataset, tends to underestimate the amount of large-scale (not formed via deep convective processes) precipitation compared to ground-based measurements (Dai, 2023). Thus, our following analysis will mainly capture the diurnal cycle of deep convective processes. Figure 5 depicts the regionally averaged diurnal cycles of precip from ERA5 and IMERG in the period 2018 - 2023. Overall we see that ERA5 captures the diurnal cycle of precip better over ocean than over land ($\max[\text{ERA5} - \text{IMERG}] > 0.1$ $\text{mm}\,\text{hr}^{-1}$ in all seasons except boreal summer). Despite a small positive bias of around 0.03 $\text{mm}\,\text{hr}^{-1}$ of ERA5 seen in all seasons compared to IMERG, the phase of the precip diurnal cycles in ERA5 agrees well with the satellite observations within

https://doi.org/10.5194/egusphere-2026-3869
Preprint. Discussion started: 31 July 2026

the North Pacific, the Tropical Pacific and Tropical Indian boxes. Over these three ocean areas the diurnal cycle of precip peaks at around 3 - 6 LST. This late night or early morning peak is present in all seasons in ERA5 and IMERG. Over the tropical ocean boxes the difference in the peak time between IMERG and ERA5 is within ±2 hours.

A similarly good agreement of the diurnal precip peak over tropical oceans away from the continents or larger islands can be found in maps across all seasons (Fig. S3). Here, the differences in the peak time of the diurnal cycle of precip along the ITCZ over the Atlantic, Pacific and Indian Ocean and the SPCZ are in general well confined within ±5 hours. However, the biases of ERA5 in the peak time remarkably increase in the proximity of islands or continents, which is in agreement with the results of Dai (2023) and can be seen in the Maritime Continent box. IMERG has a pronounced late night or early morning peak at around 3 LST, which is followed by a diurnal precip minimum from 6 to 18 LST. In contrast, ERA5 shows on average a diurnal cycle with two peaks over this region. Similar to IMERG, ERA5 captures the 3 to 5 LST peak driven by ocean grid cells. A second diurnal precip peak in ERA5 is occurring during the afternoon at around 15 LST in all seasons. This afternoon peak is caused by deep convective processes over the Indonesian and Philippine Islands (Fig. S3). Comparing ERA5 to IMERG in peak time maps, we recognize that IMERG tends to have a late night peak (0 - 5 LST) over center regions of the islands and along the shoreline an afternoon peak (Fig. S3). In contrast, ERA5 has just an afternoon precipitation peak over these large islands.

In the South America and Africa boxes (Fig. 5) ERA5's diurnal cycle of precip shows similar differences with respect to IMERG. Here, ERA5 overestimates the diurnal amplitude in particular due to the more pronounced afternoon precip peak at around 16 LST over Africa and between 14 to 16 LST depending on the season (Fig. S2). IMERG shows semidiurnal variability (with two peaks and two minima) in precip especially during winter and spring in the South America and Africa boxes. During these seasons precip peaks at around 15 LST in IMERG with an up to 0.2 $\mathrm{mm\,hr^{-1}}$ smaller diurnal precip compared to ERA5. Towards the late afternoon and early evening precip is slowly decreasing in IMERG in all seasons but without the drastic drop of around -0.3 $\mathrm{mm\,hr^{-1}}$ between 15 and 20 LST seen for ERA5. After 21 LST the diurnal precip increases again in IMERG during winter and reaches a secondary maximum at around midnight. This secondary peak of diurnal precip is also present in ERA5 but the respective peak is delayed by around 4 hours towards the early morning in the Africa and South America boxes (Fig. 5). Again, the peak time and diurnal amplitude maps help us to find a potential explanation for the too strong diurnal cycle of precip in ERA5 and the delayed secondary peak during winter and spring compared to IMERG: ERA5 overestimates the diurnal precip amplitude in the majority of the grid cells within the South America and Africa boxes (Fig. S2) with respect to IMERG. Focusing on the peak time maps of precip in ERA5 and IMERG (Fig. S3), the reanalysis product exhibits too small spatial variability with peak times between noon and 17 LST throughout all seasons. In contrast, IMERG reflects similar to CCIC for FWP a clear influence of topography on the diurnal cycle of precip, which is clearly damped in ERA5 in the tropical land boxes. In IMERG, we see areas with nighttime peaks at around 0 LST in the proximity of the Andes, the Venezuelan high lands and the mountain ranges around the Congo basin in all seasons (Fig. S3).

As described above ERA5 does not fully capture the influence of regional topographic features over tropical continents on FWP and precip. Thus, it is intuitive to wonder whether ERA5 captures the influence of topography on the diurnal cycle of HCC as it is expected to be connected to FWP and precip.

https://doi.org/10.5194/egusphere-2026-3869
Preprint. Discussion started: 31 July 2026

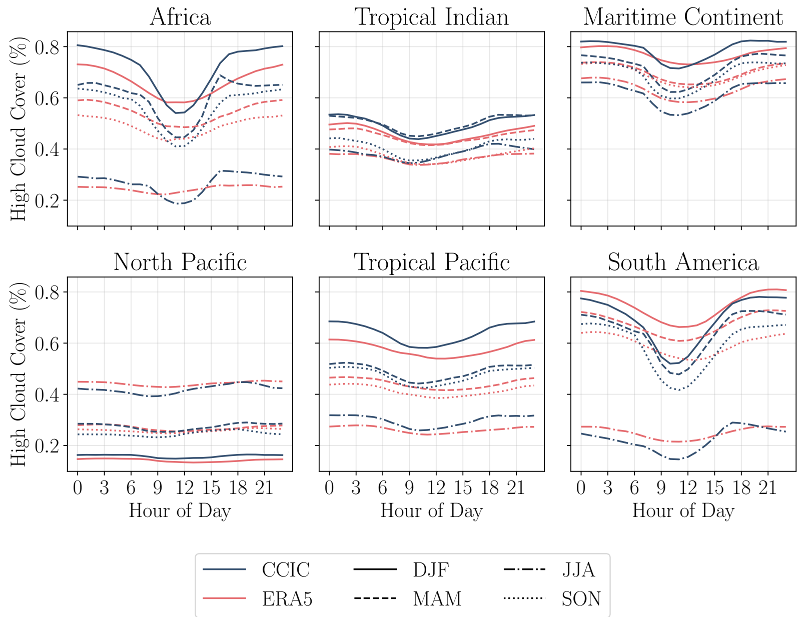

Figure 6. Regionally averaged diurnal cycles of high cloud cover from CCIC (blue) and ERA5 (red), shown for the four seasons in 2018. Regions are defined in Fig. 4.

Figure 6 shows the averaged diurnal cycle of HCC in the six tropical boxes from CCIC and ERA5 for all seasons of the year 2018. In agreement with previous findings (Dai, 2023), we see that seasonal variations in HCC are dominating diurnal variations (the differences in HCC between the seasons are substantially larger than the diurnal amplitude). This is not surprising as the main driver of HCC in all tropical boxes except the North Pacific is the seasonal shift of the ITCZ and related deep convection. This seasonal signal is well captured in ERA5, as we see for both CCIC and ERA5 that the warm and wet season (DJF in all boxes except the North Pacific, Figs. 5, 6) corresponds to the highest HCC and the cold and dry season (JJA in most boxes except the North Pacific and Tropical Indian) to the lowest HCC. In general, ERA5 tends to have a slightly smaller (ERA5 - CCIC $\sim$ -2%) HCC compared to CCIC in the Africa, Tropical Pacific, Tropical Indian and the Maritime Continent boxes throughout all seasons with the largest negative biases seen in the Africa box with maximum -5%. In the North Pacific and South America boxes ERA5 has a marginally larger (ERA5 - CCIC $\sim$ 2%) HCC during the warm season compared to CCIC. Focusing on the differences of the diurnal cycle curves, CCIC's HCC has usually higher values during the evening and nighttime and lower values in the morning until the early afternoon ($\sim$ 15 LST) in all seasons. The pronounced decrease in HCC in CCIC by up to 20 % after sunrise during the warm season over land area is underestimated in ERA5. The weak diurnal variability in HCC from ERA5 over land may be related to the fact that ERA5's HCC is dominated by the IFS convection scheme (Bechtold et al., 2014), which cannot be directly assimilated. This results in known large positive (up to $\sim$ 20 - 30 %) HCC biases of ERA5 compared to other satellite observations over the Congo basin and Amazonia (Wright et al., 2020). Over the tropical ocean boxes the diurnal amplitude of HCC from CCIC is comparably smaller than over land (2% over ocean

https://doi.org/10.5194/egusphere-2026-3869
Preprint. Discussion started: 31 July 2026

vs. 10% over land), resulting in the diurnal biases of ERA5 also being smaller. Despite the smaller decrease in HCC in the morning hours over land in ERA5, we see that the diurnal cycle of CCIC and ERA5 are in general in phase. This is surprising having in mind the large phase differences and varying strength of diurnal and sub-diurnal variability in FWP or precip over the tropical boxes between CCIC, IMERG and ERA5. One explanation is the smaller influence of topography on HCC and thus less spatial variability in CCIC's HCC peak, trough (= occurrence of the diurnal minimum) time and diurnal amplitude maps (Figs. S4-S7) within the analysed tropical boxes.

As a next step we will analyze how well km-scale models capture the diurnal cycle of FWP and precip compared to satellite observations and ERA5.

4.3 Comparison with km-scale models

To compare the diurnal cycle of CCIC and IMERG against km-scale models of the DYAMOND winter ensemble, we restrict the analysis to February 2020 and exclude HCC from the analysis. 3D cloud cover fields were not saved in the DYAMOND winter experiment (Stevens et al., 2019) and in only a few cases total cloud cover. Thus we restrict the analysis to FWP and precip and focus mainly on the box-averaged diurnal cycles due to the large inter-model spread of the DYAMOND ensemble seen for the zonal averages of FWP and precip (Fig. 1).

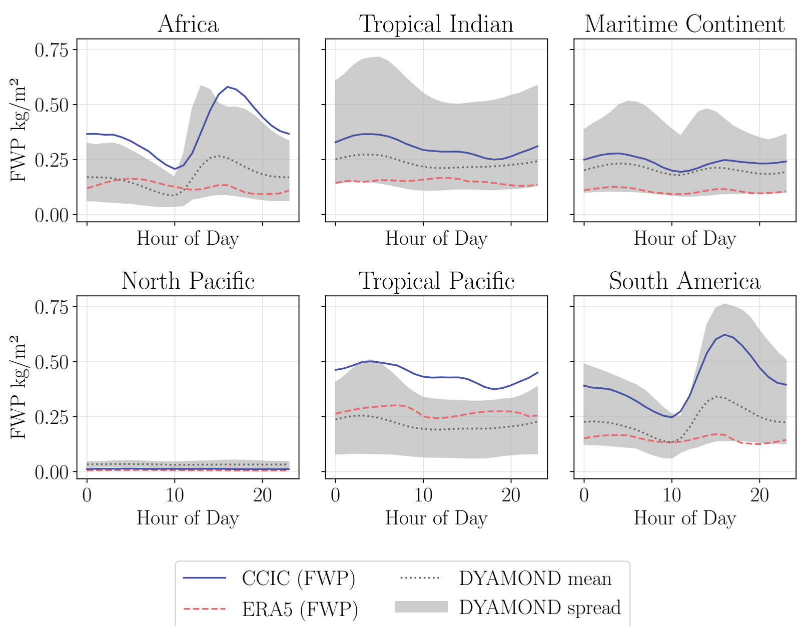

Figure 7. Regionally averaged diurnal cycles of FWP from CCIC (solid blue), ERA5 (dashed red) and DYAMOND models in February 2020. DYAMOND models are represented by the spread from minimum to maximum (gray area) and the multi-model mean (dotted gray). Regions are defined in Fig. 4.

https://doi.org/10.5194/egusphere-2026-3869
Preprint. Discussion started: 31 July 2026

Figure 7 shows the regionally averaged diurnal cycles of FWP from CCIC, ERA5 and the multi-model mean of the DYAMOND ensemble in the six tropical boxes in February 2020. In addition, we added the inter-model spread given as minimum and maximum values for each LST hour as an uncertainty estimate for DYAMOND. The multi-model average captures the diurnal cycle of FWP well in the Tropical Indian, Maritime Continent and North Pacific boxes. For the first two boxes the mean of the DYAMOND models marginally underestimates FWP compared to CCIC with around - 0.05 $\mathrm{kg\,m^{-2}}$ lower FWP, while there is a small positive bias (0.02 $\mathrm{kg\,m^{-2}}$) over the North Pacific. In agreement with previous results (Fig. 1), the multi-model mean of DYAMOND underestimates the FWP maximum in the SPCZ in the Tropical Pacific box with a negative bias of around -0.2 $\mathrm{kg\,m^{-2}}$. Similarly, the DYAMOND multi-model mean does not capture the satellite observed diurnal cycle in amplitude or phase in this region. We see this underestimation of FWP to a lesser extent also in the Africa and South America boxes. Over South America, CCIC's FWP is within the inter-model spread of the DYAMOND models, whereas in Africa, CCIC's FWP tends to be 0.05 $\mathrm{kg\,m^{-2}}$ larger than the maximum member of the DYAMOND ensemble. Despite the negative bias of more than -0.1 $\mathrm{kg\,m^{-2}}$ between the DYAMOND multi-model mean and CCIC, we see that the diurnal cycle of the DYAMOND models is similar to the one from CCIC with a too early diurnal peak by about 3 hours but a well captured FWP minimum around noon in the tropical Africa and South America boxes. Similar to the zonal averages of FWP (Fig. 1) we see a large diurnal inter-model spread within the DYAMOND ensemble of around 0.25 $\mathrm{kg\,m^{-2}}$ in the boxes that are situated along the wintertime ITCZ and the SPCZ.

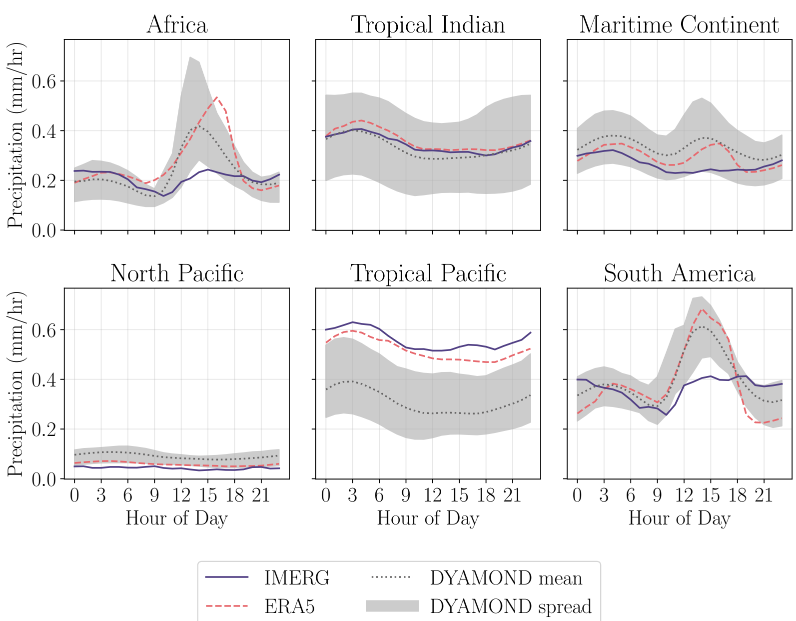

Figure 8. Regionally averaged diurnal cycles from IMERG (solid purple), ERA5 (dashed red) and the DYAMOND models in February 2020. DYAMOND models are represented by the inter-model spread from minimum to maximum (gray area) and the multi-model mean (dotted gray). Regions are defined in Fig. 4.

https://doi.org/10.5194/egusphere-2026-3869
Preprint. Discussion started: 31 July 2026

Figure 8 depicts the regionally averaged diurnal cycle of precip in February 2020 in the six tropical boxes from IMERG, ERA5 and the DYAMOND models. Similar to our findings for FWP, we see within the Tropical Indian, North Pacific and the Maritime Continent boxes smaller biases between the satellite-observed and km-scale modeled diurnal cycle curves of maximum 0.1 $\mathrm{mm\,hr^{-1}}$ (Fig. 8). Over the Tropical Indian Ocean the multi-model mean of DYAMOND is generally in-phase with IMERG with a small bias of around -0.05 $\mathrm{mm\,hr^{-1}}$ occuring in the morning hours. In the North Pacific box the multi-model mean of DYAMOND shows a wet bias compared to IMERG of approximately 0.05 $\mathrm{mm\,hr^{-1}}$. The DYAMOND models show a diurnal cycle of precip with an early-morning peak at around 6 LST similar to ERA5, which is out-of phase with IMERG that has a negligible diurnal variability in the North Pacific box (Fig. 8). In the Maritime Continent box with its strong spatial variability due to the interplay of ocean, land area and topography (Fig. S9b) the multi-model mean of DYAMOND models capture the early morning peak at 4 LST over ocean grid cells but overestimates the dominance of the afternoon peak at 14 / 15 LST over too many land area grid cells compared to to IMERG. Since the diurnal curves of ERA5 and IMERG are similar over the full time period (Fig. 5) and February 2020 (Fig. 8), we hypothesize that the DYAMOND models struggle to simulate sufficiently night-time topography related precip convection in the centers of the Indonesian Islands at around 0 LST similar to ERA5 that we see in the satellite observations (Figs. S3, S9b). In the Tropical Pacific box the DYAMOND models have the largest biases in FWP and precip compared to CCIC and IMERG. Even the maximum ensemble member from DYAMOND underestimates the diurnal precip of IMERG in the SPCZ. Quantitatively, the dry bias between the DYAMOND multi-model mean and IMERG is between -0.20 $\mathrm{mm\,hr^{-1}}$ and -0.25 $\mathrm{mm\,hr^{-1}}$ in this region. A marginally smaller bias in magnitude of around -0.20 $\mathrm{mm\,hr^{-1}}$ exists between ERA5 and DYAMOND. Besides these large biases in modelled precip on monthly scales, the biases in phase and amplitude of the diurnal cycles are small over the Tropical Pacific. All curves have a diurnal peak at around 3 LST and show weaker diurnal precip during noon and in the afternoon.

Over the tropical continents IMERG is within the inter-model spread of the DYAMOND km-scale models except during the period from 9 / 12 LST to 17 / 15 LST in the South America / Africa box when the simulated precip diurnal peak occurs. During these periods the DYAMOND multi-model mean shows a wet bias compared to IMERG of 0.15 $\mathrm{mm\,hr^{-1}}$ over Africa and 0.20 $\mathrm{mm\,hr^{-1}}$ over South America. Similar to the DJF precip diurnal cycle, we see that IMERG has an around two times smaller diurnal amplitude in February 2020 compared to ERA5, while the diurnal amplitude of the multi-model mean of DYAMOND is at least 1.5 times larger. Pfreundschuh et al. (2022) analyzed the diurnal cycle from IMERG and rain gauges for December 2020 over Brazil and found good agreement between them. Since the amplitude of the diurnal cycle of precip in Fig. 8 for February 2020 is comparable to theirs in December, this suggests that the overestimation of the diurnal amplitude in DYAMOND and ERA5 is a model bias. Similar to the DJF diurnal cycle (Fig. 5), IMERG shows two diurnal peaks in the Africa and South America boxes in February. The DYAMOND models simulate the afternoon peak over Africa 2 hours too early and over South America at least 1 hour too early with respect to IMERG. The midnight peak in IMERG is delayed in DYAMOND models by about 3 hours in both the Africa and South America boxes.

In the next section we will discuss key results of our comparison between satellite observations, ERA5 and km-scale models. In addition, we compare the diurnal cycles in CCIC variables and IMERG and discuss potential drivers of the distinct diurnal cycles over tropical land and ocean boxes.

https://doi.org/10.5194/egusphere-2026-3869
Preprint. Discussion started: 31 July 2026

5 Discussion

5.1 Performance of km-scale models in simulating diurnal cycles

Km-scales models reduce substantially the underestimation of the zonally averaged FWP compared to CMIP6 models (Eriksson et al., 2026). However, the DYAMOND winter simulations used in this study exhibit a bias in capturing the position of the ITCZ in precip in February 2020 compared to satellite observations. While satellite observations in FWP and precip show a maximum south of the Equator at around 10 °S (Fig. 1b), the DYAMOND models simulate the maximum in precip north of the Equator at 5 °N (Fig. 1d), despite large similarities between DYAMOND and satellite observations in zonally averaged FWP in the tropics (Fig. 1b). The bias of the DYAMOND models in representing the tropical circulation, that also In and Khairoutdinov (2026) recently investigated, is further visible in the simulated diurnal cycles in the six tropical regions analysed in this manuscript. We see a generally good agreement in the diurnal phase and amplitude of FWP between the DYAMOND multi-model mean and CCIC in three of the four tropical ocean boxes. However, for precip this holds true for just one out of four tropical ocean boxes. Especially, over the SPCZ in the Tropical Pacific box we find a pronounced underestimation of precip of -0.25 $\mathrm{mm\,hr^{-1}}$ and FWP of around -0.20 $\mathrm{kg\,m^{-2}}$ resulting in a reduced performance of the DYAMOND models in capturing the diurnal amplitude and phase of the satellite-observed diurnal cycle in this region. In the two tropical land boxes the DYAMOND models underestimate the diurnal amplitude of FWP but overestimate the amplitude of precip. A potential reason for this may be a less heterogeneous modeled diurnal cycle in peak times on grid-scale level in km-scale models (Figs. S8, S9) due to the underestimated influence of topography and of mesoscale convective systems in the DYAMOND simulations (Eriksson et al., 2026). In addition large uncertainties in the underlying simulated convective and parameterized subgrid processes (e.g. microphysics) in DYAMOND (e.g. Mooers et al., 2023; In and Khairoutdinov, 2026; Song et al., 2024) may play a role for the overestimation of the diurnal cycle of precipitation over tropical land areas.

Thus, our results show that simulated tropical diurnal cycles from the DYAMOND km-scale models exhibit larger diurnal amplitude differences with respect to satellite observations over land than over the oceans, which is in agreement with Song et al. (2024) but for precip. It has to be noted, though, that since the DYAMOND winter project in 2020/21 some of the participating km-scale models underwent developments of their subgrid parameterizations (e.g. Hohenegger et al., 2023; Kroll et al., 2025; Segura et al., 2025), which may potentially result in smaller uncertainties and biases of the simulated diurnal cycles of FWP and precip compared to satellite observations. Numerical models with resolved deep convective processes such as km-scale models often provide more realistic diurnal cycles in tropical latitudes compared to state-of-the-art climate models with parameterized convection (e.g. Behrens et al., 2025).

5.2 Satellite-observed diurnal cycle of deep convection

As a final step, we combine the diurnal cycles of FWP, HCC from CCIC with the diurnal cycle of precip from IMERG within the six tropical grid boxes. Figure 9 depicts the box-averaged diurnal cycle of FWP and precip for the period 2018-2023. The seasons of 2018 showing the diurnal cycles of FWP, HCC and precip are shown in the supplement (Fig. S10-S13).

https://doi.org/10.5194/egusphere-2026-3869
Preprint. Discussion started: 31 July 2026

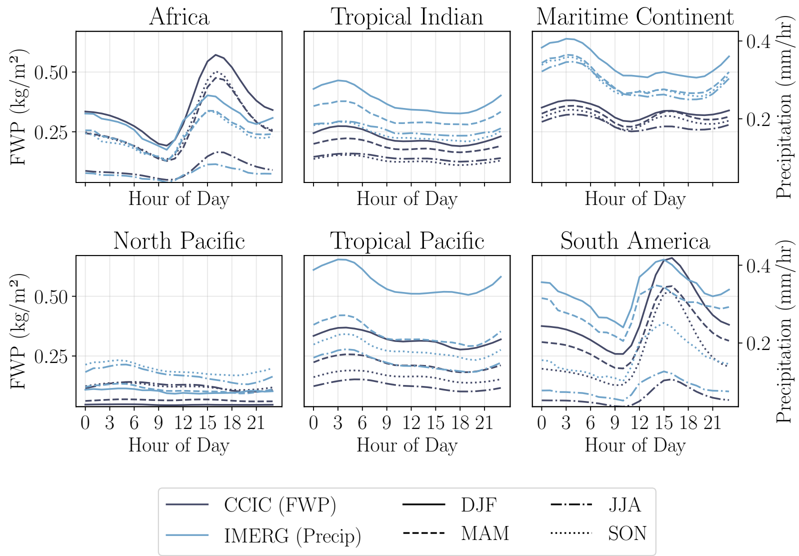

Figure 9. a) Regional diurnal cycles of FWP from CCIC (dark blue) and precipitation from IMERG (light blue), shown for the four seasons in the period 2018-2023. The regions are defined in Fig. 4.

The regionally averaged diurnal cycles of precip and FWP show in general a strong synchronicity with marginal phase shifts of peak times of around ±1 h in all tropical boxes throughout all seasons (Fig. 9). Over ocean FWP and precip are generally in phase, while over land FWP trails behind precip by around 1 h. We also see that the regionally averaged diurnal cycle of HCC is shifted compared to FWP and precip over both land and ocean areas. HCC is influenced mainly by diurnal variability, while FWP and precip have a stronger influence by semidiurnal variability.

Over tropical land areas the afternoon peak of regionally averaged diurnal precip occurs before the one for FWP, which follows with a lag of up to 1-2 hours. To explain this phase shift an inspection of diurnal amplitude and peak time maps is necessary. In these maps, precip has a stronger 12 h (and finer) variability that results in more heterogeneous peak time distributions (Fig. S3) compared to FWP (Fig. S1). For FWP we see a pronounced bimodality of either nighttime topography related diurnal peaks or regular late afternoon peaks with a clear separation between the regimes in peak time maps within the South America and Africa boxes (Fig. S1). For precip, we see more characteristic diurnal convective regimes. The afternoon peak in precip occurs often two hours earlier at around 15 LST (Fig. S3). The orographic nighttime regime of precip is found at more grid cells than for FWP. In the precip peak time maps it is further visible how deep convection propagates from the mountain ranges (e.g. the Andes or the Venezuelan highlands) with the large-scale circulation into lower-lying neighboring areas over the course of the night and in the early morning (Fig. S3). This nighttime propagation is less pronounced in FWP (Fig. S1). Similarly, the signature of mesoscale convective systems with night-time peaks in precip over lower-lying western Amazonia is not as pronounced in FWP during the wet season (Figs. 3,S3). All these effects contribute to the slightly shifted regionally averaged precip diurnal cycle with stronger 12 h (and finer) variability than in FWP in the tropical land boxes. The

https://doi.org/10.5194/egusphere-2026-3869
Preprint. Discussion started: 31 July 2026

regionally averaged diurnal HCC (Figs. S10-S13) starts to increase in the late morning at about 10 / 11 LST and continues to rise after precip and FWP reach their afternoon peaks over tropical land in all seasons. Diurnal HCC culminates in a broad nighttime peak from the late evening to midnight during wintertime (the warm and wet season), while it occurs in the early evening during summertime (the dry season) with a smaller diurnal amplitude. For HCC the peak time geographical distributions indicate two pronounced diurnal convective regimes over tropical land areas. An after midnight diurnal HCC regime that is related to orography and a late evening regime over mostly low-lying areas during the wintertime (Figs. S5,S6). During summertime late evening peaks are dominating over tropical land. Our findings agree with previous literature that HCC peaks after the diurnal precip peak and persists long after the maximum of convective processes over land (Ćorko et al., 2025). In contrast to Dai (2023) we find in regional boxes over land a pronounced diurnal amplitude of HCC, which cannot be seen in the entire tropical latitudinal band shown in Dai (2023).

In the tropical oceans boxes except the North Pacific box we see a strong synchronicity of diurnal precip and diurnal FWP independent of the seasons with an early morning peak at around 3 to 5 LST. Over the North Pacific precip has a similar early morning peak but FWP does not show a pronounced diurnal variability like precip. Thus, the diurnal variability of precip is not predominantly originating from deep convective processes involving the formation of frozen particles within the North Pacific box. Over the Maritime Continent FWP and precip are synchronous with each other with an early morning over ocean grid cells and inland topography related peak and a small secondary afternoon peak occurring along the shorelines of the Indonesian archipelago (Figs. S1,S3).

6 Conclusions

In this paper we compare the diurnal cycles of frozen water path and precipitation from satellite observations, the ERA5 reanalysis and simulations from km-scale models (DYAMOND). We use the machine learning based CCIC satellite dataset (Table 1) for frozen water path and high cloud cover, the IMERG product (Table 1) is used for precipitation. CCIC and IMERG have a nominal resolution well within the deep convective gray zone (below 10 km) and finer and thus allow for a direct comparison with km-scale models. For comparison we utilize the ERA5 reanalysis (Table 1) and output from the DYAMOND winter km-scale model ensemble (Tables 1,S1).

As a first step we conduct a zonal average analysis of frozen water and precipitation to ensure comparability of the respective diurnal cycles. For frozen water path we find a good agreement of zonal structures between CCIC, km-scale models and ERA5 in the tropics, despite a general underestimation of frozen water path in ERA5 (Eriksson et al., 2026; Pfreundschuh et al., 2025). Km-scale models show a general underestimation of frozen water path in the boreal mid latitudes during wintertime compared to the satellite observations. For precipitation, km-scale models show biases related to the position of the ITCZ and a too weak SPCZ during wintertime compared to the observations, while ERA5 agrees well with the satellite observed zonal averages.

The regionally averaged diurnal cycle of frozen water path in CCIC is in good agreement with previous work that focused on upper-tropospheric ice water content in the tropics with afternoon peaks over tropical land and early morning peaks over ocean

https://doi.org/10.5194/egusphere-2026-3869
Preprint. Discussion started: 31 July 2026

(Eriksson et al., 2014). ERA5 underestimates, both in absolute and relative terms, the diurnal amplitude of frozen water path over tropical land areas in all seasons compared to CCIC. Furthermore, ERA5 shows a delay of up to 6 hours over Amazonia, the Congo basin and the SPCZ compared to CCIC in peak time maps that is mostly pronounced during the respective warm and wet season. For precipitation, ERA5 overestimates the diurnal amplitudes over Amazonia and the Congo Basin in all seasons. With respect to the diurnal phase, ERA5 agrees well with IMERG but underestimates the occurrences of nighttime precipitation peaks due to topography and mesoscale convective systems over South America and Africa during the warm and wet season. For high cloud cover, the diurnal cycles of CCIC and ERA5 are mostly in phase in the tropics. However, ERA5 underestimates the reduction in high cloud cover around noon over tropical land areas most pronounced over Amazonia and the Congo basin during wintertime, e.g. the respective warm and wet season.

The DYAMOND km-scale models show an improved diurnal cycle for precipitation in the tropics with small regionally averaged phase biases in the order of 1-2 hours too early. In contrast, the reported diurnal phase biases of many ESMs are in order of four and more hours for precipitation (e.g. Christopoulos and Schneider, 2021; Song et al., 2024; Behrens et al., 2025). Despite these advances, substantial biases are present in diurnal amplitudes, especially over tropical land areas, compared to CCIC for frozen water path and IMERG for precipitation. Over Amazonia and the Congo Basin, the km-scale models underestimate the diurnal amplitudes of frozen water path, while they overestimate the diurnal amplitudes of precipitation. In addition, the simulated diurnal cycles of frozen water path and precipitation over the SPCZ exhibit large biases due to a general underestimation of frozen water path and precipitation over this region compared to satellite observations.

Diurnal cycle analyses based on high-resolution satellite products like CCIC or IMERG enable a more detailed evaluation of the simulated convective processes in km-scale models compared to the coarser ERA5 reanalysis. Moreover, high-resolution products with high temporal and spatial resolution allow to differentiate between persistent systematic biases and diurnally varying biases in km-scale models. Our diurnal analysis indicates that the biases of km-scale models over the SPCZ are attributable to persistent systematic biases in km-scale models with virtually none diurnal variability. In contrast, the mismatch in the diurnal amplitude of frozen water path and precipitation over tropical land areas in km-scale models points to differences in the simulated convective processes themselves, e.g. convective triggering, processes underlying the formation of mesoscale convection or precipitation efficiency (Kukulies et al., 2026) compared to km-scale satellite observations.

Cross-evaluation of km-scale satellite datasets allows a more detailed look at the diurnal cycle of deep convective processes. The regionally-averaged diurnal cycles of frozen water path and precipitation over tropical oceans peak at the same time during all seasons. The delay of the diurnal cycle of the regionally averaged frozen water path of one hour over tropical land can be explained by less spatial variability in peak time maps of frozen water path compared to precipitation. For precipitation we find a stronger imprint of mesoscale convective systems and the migration of convective systems with the large-scale circulation. High cloud cover with the smallest spatial diurnal variability in peak time maps, peaks usually a few hours later, with the largest delay compared to precipitation and frozen water path during the respective warm and wet season.

Our analysis illustrates that combining different satellite datasets helps to understand regional diurnal cycles of deep convective processes even on a grid-scale level and to investigate persistent and diurnal biases of km-scale models. This approach can also be applied to the upcoming next generation ESMs and helps to alleviate longstanding diurnal biases caused by their parameterized deep convective processes.

Code and data availability. The code to create all figures, tables of this manuscript is openly available and archived with zenodo (Leko et al., 2026). We archived the preprocessed CCIC, IMERG, ERA5 and DYAMOND data to reproduce all figures and findings of this study on zenodo (Behrens et al., 2026). DYAMOND model output is available on the DKRZ (https://easy.gems.dkrz.de/DYAMOND/Winter/index.html, last access: 30 June 2026). ERA5 data was downloaded via the Copernicus Climate Data Store (Copernicus Climate Change Service, 2023). Chalmers Cloud Ice Climatology (CCIC) can be downloaded from https://registry.opendata.aws/ccic (Amell and Pfreundschuh, 2025).2C-ICE data (Deng et al., 2025) was downloaded from the CloudSat Dataprocessing Center. DARDAR-CLOUD v3-10 ((https://doi.org/10.25326/449, Delanoë and Hogan, 2025)) data is at the ICARE Data and Services Center. IMERG version 7 (Huffman et al., 2023a) data for this paper was accessed and downloaded through the NASA Earthdata portal.

Author contributions. LL conducted the diurnal cycle analysis and visualization of the results. GB and LL lead the writing of the manuscript. AA and NM lead the data collection for the diurnal cycle analysis. PE, GB and AL supervised this research project. All authors contributed to the writing and discussion of the manuscript.

Competing interests. There are no competing interests.

Acknowledgements. The work of AA and PE has been supported by the European Union's HORIZON Research and Innovation Programme under Grant 101120657, project ENFIELD (European Lighthouse to Manifest Trustworthy and Green AI). This work used resources of the Deutsches Klimarechenzentrum (DKRZ) granted by its Scientific Steering Committee (WLA) under project IDs 0854 (Erdsystemmodelle-valuierung), 1179 (USMILE) and 1083 (Climate Informatics). DYAMOND data management was provided by the German Climate Computing Center (DKRZ) and supported through the projects ESiWACE and ESiWACE2. The projects ESiWACE and ESiWACE2 have received funding from the European Union's Horizon 2020 research and innovation programme under grant agreements No 675191 and 823988. We would like to thank Tom Beucler and Lucile Ricard for initial help understanding differences in the units of the saved precipitation variables of the DYAMOND km-scale models.

https://doi.org/10.5194/egusphere-2026-3869
Preprint. Discussion started: 31 July 2026

References

Amell, A., Pfreundschuh, S., and Eriksson, P.: The Chalmers Cloud Ice Climatology: retrieval implementation and validation, Atmospheric Measurement Techniques, 17, 4337–4368, https://doi.org/10.5194/amt-17-4337-2024, 2024.

Amell, A., Hee, L., Pfreundschuh, S., and Eriksson, P.: Probabilistic Near-Real-Time Retrievals of Rain Over Africa Using Deep Learning, Journal of Geophysical Research: Atmospheres, 130, e2025JD044 595, https://doi.org/10.1029/2025JD044595, e2025JD044595 2025JD044595, 2025.

Amell, A., Pfreundschuh, S., and Eriksson, P.: Fine-tuning a machine-learned 3D cloud climatology reveals aspects of cloud cover trends, ESS Open Archive, 2026, https://doi.org/10.22541/essoar.15001993/v1, 2026.

Bechtold, P., Semane, N., Lopez, P., Chaboureau, J.-P., Beljaars, A., and Bormann, N.: Representing Equilibrium and Nonequilibrium Convection in Large-Scale Models, Journal of the Atmospheric Sciences, 71, 734 – 753, https://doi.org/10.1175/JAS-D-13-0163.1, 2014.

Behrens, G., Beucler, T., Iglesias-Suarez, F., Yu, S., Gentine, P., Pritchard, M., Schwabe, M., and Eyring, V.: Simulating Atmospheric Processes in Earth System Models and Quantifying Uncertainties With Deep Learning Multi-Member and Stochastic Parameterizations, Journal of Advances in Modeling Earth Systems, 17, e2024MS004 272, https://doi.org/10.1029/2024MS004272, e2024MS004272 2024MS004272, 2025.

Behrens, G., Leko, L., Amell, A., and Müller, N.: Data for : Diurnal Cycles of Deep Convective Processes in Satellite Measurements, the ERA5 Reanalysis and DYAMOND km-scale Models [Dataset], https://doi.org/10.5281/zenodo.20842368, 2026.

Christopoulos, C. and Schneider, T.: Assessing Biases and Climate Implications of the Diurnal Precipitation Cycle in Climate Models, Geophysical Research Letters, 48, e2021GL093 017, https://doi.org/10.1029/2021GL093017, e2021GL093017 2021GL093017, 2021.

Copernicus Climate Change Service: Complete ERA5 global atmospheric reanalysis [Dataset], https://doi.org/10.24381/CDS.143582CF, 2023.

Covey, C., Gleckler, P. J., Doutriaux, C., Williams, D. N., Dai, A., Fasullo, J., Trenberth, K., and Berg, A.: Metrics for the Diurnal Cycle of Precipitation: Toward Routine Benchmarks for Climate Models, 29, 4461–4471, https://doi.org/10.1175/JCLI-D-15-0664.1, 2016.

Dai, A.: Precipitation Characteristics in Eighteen Coupled Climate Models, Journal of Climate, 19, 4605 – 4630, https://doi.org/10.1175/JCLI3884.1, 2006.

Dai, A.: The diurnal cycle from observations and ERA5 in surface pressure, temperature, humidity, and winds, Climate Dynamics, 61, 2965–2990, https://doi.org/10.1007/s00382-023-06721-x, 2023.

Delanoë, J. and Hogan, R. J.: Combined CloudSat-CALIPSO-MODIS retrievals of the properties of ice clouds, Journal of Geophysical Research: Atmospheres, 115, https://doi.org/10.1029/2009JD012346, 2010.

Delanoë, J. and Hogan, R. J.: DARDAR-cloud V3-10 [Dataset], AERIS/ICARE Data and Services Center, https://doi.org/10.25326/449, last access: 29 June 2026, 2025.

Deng, M., Mace, G. G., Wang, Z., and Berry, E.: CloudSat 2C-ICE product update with a new Ze parameterization in lidar-only region, Journal of Geophysical Research: Atmospheres, 120, 12,198–12,208, https://doi.org/10.1002/2015JD023600, 2015.

Deng, M., Mace, G. G., Wang, Z., and Berry, E.: 2C-ICE P1_R05 [Dataset], CloudSat Dataprocessing Cente, https://www.cloudsat.cira.colostate.edu/data-products/2c-ice, last access: 29 June 2026, 2025.

Eriksson, P., Rydberg, B., Johnston, M., Murtagh, D. P., Struthers, H., Ferrachat, S., and Lohmann, U.: Diurnal variations of humidity and ice water content in the tropical upper troposphere, Atmospheric Chemistry and Physics, 10, 11 519–11 533, https://doi.org/10.5194/acp-10-11519-2010, 2010.

https://doi.org/10.5194/egusphere-2026-3869
Preprint. Discussion started: 31 July 2026

Eriksson, P., Rydberg, B., Sagawa, H., Johnston, M. S., and Kasai, Y.: Overview and sample applications of SMILES and Odin-SMR retrievals of upper tropospheric humidity and cloud ice mass, Atmospheric Chemistry and Physics, 14, 12 613–12 629, https://doi.org/10.5194/acp-14-12613-2014, 2014.

Eriksson, P., Baró Pérez, A., Müller, N., Hallborn, H., May, E., Brath, M., Buehler, S. A., and Ickes, L.: Advancements and continued challenges in observations and global modelling of atmospheric ice mass, Atmospheric Chemistry and Physics, 26, 2741–2768, https://doi.org/10.5194/acp-26-2741-2026, 2026.

Gong, J., Zeng, X., Wu, D. L., and Li, X.: Diurnal Variation of Tropical Ice Cloud Microphysics: Evidence from Global Precipitation Measurement Microwave Imager Polarimetric Measurements, Geophysical Research Letters, 45, 1185–1193, https://doi.org/10.1002/2017GL075519, 2018.

Hersbach, H., Bell, B., Berrisford, P., Hirahara, S., Horányi, A., Muñoz-Sabater, J., Nicolas, J., Peubey, C., Radu, R., Schepers, D., Simmons, A., Soci, C., Abdalla, S., Abellan, X., Balsamo, G., Bechtold, P., Biavati, G., Bidlot, J., Bonavita, M., De Chiara, G., Dahlgren, P., Dee, D., Diamantakis, M., Dragani, R., Flemming, J., Forbes, R., Fuentes, M., Geer, A., Haimberger, L., Healy, S., Hogan, R. J., Hólm, E., Janisková, M., Keeley, S., Laloyaux, P., Lopez, P., Lupu, C., Radnoti, G., de Rosnay, P., Rozum, I., Vamborg, F., Villaume, S., and Thépaut, J.-N.: The ERA5 global reanalysis, Quarterly Journal of the Royal Meteorological Society, 146, 1999–2049, https://doi.org/10.1002/qj.3803, 2020.

Hohenegger, C., Korn, P., Linardakis, L., Redler, R., Schnur, R., Adamidis, P., Bao, J., Bastin, S., Behravesh, M., Bergemann, M., Biercamp, J., Bockelmann, H., Brokopf, R., Brüggemann, N., Casaroli, L., Chegini, F., Datseris, G., Esch, M., George, G., Giorgetta, M., Gutjahr, O., Haak, H., Hanke, M., Ilyina, T., Jahns, T., Jungclaus, J., Kern, M., Klocke, D., Kluft, L., Kölling, T., Kornblueh, L., Kosukhin, S., Kroll, C., Lee, J., Mauritsen, T., Mehlmann, C., Mieslinger, T., Naumann, A. K., Paccini, L., Peinado, A., Praturi, D. S., Putrasahan, D., Rast, S., Riddick, T., Roeber, N., Schmidt, H., Schulzweida, U., Schütte, F., Segura, H., Shevchenko, R., Singh, V., Specht, M., Stephan, C. C., von Storch, J.-S., Vogel, R., Wengel, C., Winkler, M., Ziemen, F., Marotzke, J., and Stevens, B.: ICON-Sapphire: simulating the components of the Earth system and their interactions at kilometer and subkilometer scales, Geoscientific Model Development, 16, 779–811, https://doi.org/10.5194/gmd-16-779-2023, 2023.

Huffman, G., Stocker, E., Bolvin, D., Nelkin, E., and Tan, J.: GPM IMERG Final Precipitation L3 Half Hourly 0.1 degree x 0.1 degree V07 [Datatset], https://doi.org/10.5067/GPM/IMERG/3B-HH/07, last access: 29 June 2026, 2023a.

Huffman, G. J., Bolvin, D. T., Joyce, R., Kelley, O. A., Nelkin, E. J., Portier, A., Stocker, E. F., Tan, J., Watters, D. C., and West, B. J.: IMERG V07 Release Notes, 2023b.

In, J. and Khairoutdinov, M.: Evaluation of Global Storm-Resolving Models in DYAMOND-Winter: Radiation, Precipitation, Water Vapor, and Convective Organization, Journal of Advances in Modeling Earth Systems, 18, e2025MS005 258, https://doi.org/10.1029/2025MS005258, e2025MS005258 2025MS005258, 2026.

Janowiak, J. E., Joyce, R. J., and Yarosh, Y.: A Real-Time Global Half-Hourly Pixel-Resolution Infrared Dataset and Its Applications, Bulletin of the American Meteorological Society, 82, 205 – 218, https://doi.org/10.1175/1520-0477(2001)082<0205:ARTGHH>2.3.CO;2, 2001.

Jeong, J.-H., Walther, A., Nikulin, G., Chen, D., and Jones, C.: Diurnal cycle of precipitation amount and frequency in Sweden: observation versus model simulation, Tellus A: Dynamic Meteorology and Oceanography, 63, https://a.tellusjournals.se/articles/10.1111/j.1600-0870.2011.00517.x, 2011.

Kroll, C. A., Jnglin Wills, R. C., Kornblueh, L., Niemeier, U., and Schneidereit, A.: Parameterization adaption needed to unlock the benefits of increased resolution for the ITCZ in ICON, Atmospheric Chemistry and Physics, 25, 16 915–16 943, https://doi.org/10.5194/acp-25-16915-2025, 2025.

Kukulies, J., Prein, A. F., Done, J. M., Stansfield, A. M., and Rios-Berrios, R.: Precipitation Efficiency by Storm Type in km-Scale Climate Simulations and Satellite Observations, Journal of Geophysical Research: Atmospheres, 131, e2025JD044 800, https://doi.org/10.1029/2025JD044800, e2025JD044800 2025JD044800, 2026.

Leko, L.: The Diurnal Cycle of Cloud Ice Water Path, http://hdl.handle.net/20.500.12380/309563, 2025.

Leko, L., Behrens, G., Amell, A., and Müller, N.: Code for: Diurnal Cycles of Deep Convective Processes in Satellite Measurements, the ERA5 Reanalysis and DYAMOND km-scale Models [Software], https://doi.org/10.5281/zenodo.21041035, 2026.

Mooers, G., Pritchard, M., Beucler, T., Srivastava, P., Mangipudi, H., Peng, L., Gentine, P., and Mandt, S.: Comparing storm resolving models and climates via unsupervised machine learning, Scientific Reports, 13, 22 365, https://doi.org/10.1038/s41598-023-49455-w, 2023.

Pfreundschuh, S., Ingemarsson, I., Eriksson, P., Vila, D. A., and Calheiros, A. J. P.: An improved near-real-time precipitation retrieval for Brazil, Atmospheric Measurement Techniques, 15, 6907–6933, https://doi.org/10.5194/amt-15-6907-2022, 2022.

Pfreundschuh, S., Guilloteau, C., Brown, P. J., Kummerow, C. D., and Eriksson, P.: GPROF V7 and beyond: assessment of current and potential future versions of the GPROF passive microwave precipitation retrievals against ground radar measurements over the continental US and the Pacific Ocean, Atmospheric Measurement Techniques, 17, 515–538, https://doi.org/10.5194/amt-17-515-2024, 2024.

Pfreundschuh, S., Kukulies, J., Amell, A., Hallborn, H., May, E., and Eriksson, P.: The Chalmers Cloud Ice Climatology: A Novel Robust Climate Record of Frozen Cloud Hydrometeor Concentrations, Journal of Geophysical Research: Atmospheres, 130, e2024JD042 618, https://doi.org/10.1029/2024JD042618, e2024JD042618 2024JD042618, 2025.

Ricard, L., Beucler, T., Stephan, C. C., and Nenes, A.: A causal intercomparison framework unravels precipitation drivers in Global Storm-Resolving Models, npj Climate and Atmospheric Science, 8, 245, https://doi.org/10.1038/s41612-025-01104-x, 2025.

Sassen, K. and Wang, Z.: Classifying clouds around the globe with the CloudSat radar: 1-year of results, Geophysical Research Letters, 35, https://doi.org/10.1029/2007GL032591, 2008.

Schulzweida, U.: CDO User Guide, https://doi.org/10.5281/zenodo.10020800, 2023.

Segura, H., Bayley, C., Fievét, R., Glöckner, H., Günther, M., Kluft, L., Naumann, A. K., Ortega, S., Praturi, D. S., Rixen, M., Schmidt, H., Winkler, M., Hohenegger, C., and Stevens, B.: A Single Tropical Rainbelt in Global Storm-Resolving Models: The Role of Surface Heat Fluxes Over the Warm Pool, Journal of Advances in Modeling Earth Systems, 17, e2024MS004 897, https://doi.org/10.1029/2024MS004897, e2024MS004897 2024MS004897, 2025.

Song, J., Song, F., Feng, Z., Leung, L. R., Li, C., and Wu, L.: Realistic Precipitation Diurnal Cycle in Global Convection-Permitting Models by Resolving Mesoscale Convective Systems, Geophysical Research Letters, 51, e2024GL109 945, https://doi.org/10.1029/2024GL109945, e2024GL109945 2024GL109945, 2024.

Stevens, B., Satoh, M., Auger, L., Biercamp, J., Bretherton, C. S., Chen, X., Düben, P., Judt, F., Khairoutdinov, M., Klocke, D., et al.: DYAMOND: the DYnamics of the Atmospheric general circulation Modeled On Non-hydrostatic Domains, Progress in Earth and Planetary Science, 6, 1–17, https://doi.org/https://doi.org/10.1186/s40645-019-0304-z, 2019.

Tian, J., Dong, X., Xi, B., and Feng, Z.: Characteristics of Ice Cloud–Precipitation of Warm Season Mesoscale Convective Systems over the Great Plains, Journal of Hydrometeorology, 21, 317 – 334, https://doi.org/10.1175/JHM-D-19-0176.1, 2020.

Waliser, D. E., Li, J.-L. F., Woods, C. P., Austin, R. T., Bacmeister, J., Chern, J., Del Genio, A., Jiang, J. H., Kuang, Z., Meng, H., Minnis, P., Platnick, S., Rossow, W. B., Stephens, G. L., Sun-Mack, S., Tao, W.-K., Tompkins, A. M., Vane, D. G., Walker, C., and Wu, D.: Cloud ice: A climate model challenge with signs and expectations of progress, Journal of Geophysical Research: Atmospheres, 114, https://doi.org/10.1029/2008JD010015, 2009.

https://doi.org/10.5194/egusphere-2026-3869
Preprint. Discussion started: 31 July 2026

Watters, D. and Battaglia, A.: The Summertime Diurnal Cycle of Precipitation Derived from IMERG, Remote Sensing, 11, 1781, https://doi.org/10.3390/rs11151781, number: 15 Publisher: Multidisciplinary Digital Publishing Institute, 2019.

Watters, D., Battaglia, A., and Allan, R. P.: The Diurnal Cycle of Precipitation according to Multiple Decades of Global Satellite Observations, Three CMIP6 Models, and the ECMWF Reanalysis, Journal of Climate, 34, 5063 – 5080, https://doi.org/10.1175/JCLI-D-20-0966.1, 2021.

Wessinger, S. E., Rapp, A. D., and Elsaesser, G. S.: An Unexpected Peak in Daytime Convection Initiation Weakens Diurnal Amplitude of Tropical Oceanic Precipitation and Cloud Cover, Journal of Geophysical Research: Atmospheres, 130, e2025JD044 399, https://doi.org/10.1029/2025JD044399, e2025JD044399 2025JD044399, 2025.

Wright, J. S., Sun, X., Konopka, P., Krüger, K., Legras, B., Molod, A. M., Tegtmeier, S., Zhang, G. J., and Zhao, X.: Differences in tropical high clouds among reanalyses: origins and radiative impacts, Atmospheric Chemistry and Physics, 20, 8989–9030, https://doi.org/10.5194/acp-20-8989-2020, 2020.

Yang, G.-Y. and Slingo, J.: The Diurnal Cycle in the Tropics, Monthly Weather Review, 129, 784 – 801, https://doi.org/10.1175/1520-0493(2001)129<0784:TDCITT>2.0.CO;2, 2001.

Yuval, J., Langmore, I., Kochkov, D., and Hoyer, S.: Neural general circulation models for modeling precipitation, Science Advances, 12, eadv6891, https://doi.org/10.1126/sciadv.adv6891, 2026.

Ćorko, K., Burkhardt, U., Ewald, F., and Köhler, M.: Inter-Model Variability of Tropical Total Ice Water Path Simulated by the Convection Permitting DYAMOND Models, Journal of Geophysical Research: Atmospheres, 130, e2024JD041 954, https://doi.org/10.1029/2024JD041954, e2024JD041954 2024JD041954, 2025.